HHS Public Access

Author manuscript

Nat Neurosci. Author manuscript; available in PMC 2022 February 11.

Published in final edited form as:

Nat Neurosci. 2021 August ; 24(8): 1077–1088. doi:10.1038/s41593-021-00859-9.

Interactions between ALS-linked FUS and nucleoporins are associated with defects in the nucleocytoplasmic transport pathway

Yen-Chen Lin[1,#], **Meenakshi Sundaram Kumar**[1,#], **Nandini Ramesh**[2,3,#], **Eric N. Anderson**[2], **Aivi T. Nguyen**[4], **Boram Kim**[4], **Simon Cheung**[5], **Justin A. McDonough**[6], **William C. Skarnes**[6], **Rodrigo Lopez-Gonzalez**[1], **John E. Landers**[1], **Nicolas L. Fawzi**[7], **Ian R.A. Mackenzie**[5], **Edward B. Lee**[4], **Jeffrey A. Nickerson**[8], **David Grunwald**[9], **Udai B. Pandey**[2], **Daryl A. Bosco**[1,10,11,*]

[1]Department of Neurology, University of Massachusetts Medical School, Worcester, Massachusetts, MA, 01605, USA

[2]Division of Child Neurology, Department of Pediatrics, Children's Hospital of Pittsburgh, University of Pittsburgh Medical Center, Pittsburgh, PA, 15213, USA

[3]Department of Human Genetics, Graduate School of Public Health, University of Pittsburgh, PA, 15261, USA

[4]Department of Pathology and Laboratory Medicine, University of Pennsylvania, Philadelphia, PA, 19104, USA

[5]Department of Pathology, Vancouver General Hospital, Vancouver, British Columbia V5Z 1M9, Canada

[6]The Jackson Laboratory for Genomic Medicine, Farmington, CT, 06032, USA

[7]Department of Molecular Pharmacology, Physiology, and Biotechnology, Brown University, Providence, RI, 02912, USA

[8]Department of Pediatrics, University of Massachusetts Medical School, Worcester, 01605, USA

[9]RNA Therapeutics Institute, University of Massachusetts Medical School, Worcester, MA, 01605, USA

[10]Department of Biochemistry and Molecular Pharmacology, University of Massachusetts Medical School, Worcester, MA, 01605, USA

[*]To whom correspondence should be addressed: Daryl A. Bosco: Department of Neurology, University of Massachusetts Medical Center, Worcester, MA 01605; Daryl.Bosco@umassmed.edu; Tel. (774) 455-3745; Fax. (508) 856-6750.

AUTHOR CONTRIBUTIONS

Y.-C.L., M.S.K., N.R., U.B.P. and D.A.B. conceptualized and designed the project. Y.-C.L., M.S.K., N.R., E.N.A, A.T.N, B.K., S.C., J.A.M, and W.C.S conducted the experiments. Y.-C.L., M.S.K., N.R., E.N.A, A.T.N, B.K., S.C., J.A.M, W.C.S, I.R.A.M, E.B.L, J.A.N, D.G, U.B.P. and D.A.B. analyzed the data. J.E.L. and N.L.F. provided critical intellectual input. R.L.-G. reprogrammed the control iPSC line designated as C1. D.A.B. wrote the paper with co-first authors and contributions from all co-authors.

# These authors contributed equally

Code availability statement: Code used for the FRAP analysis of recombinant proteins is provided in the Supplemental_Script_FRAP.py.

DECLARATION OF INTERESTS

The authors declare no competing interests.

[11]Lead Contact

Abstract

Nucleocytoplasmic transport (NCT) decline occurs with aging and neurodegeneration. Here, we investigated the NCT pathway in models of ALS-fused in sarcoma (FUS). Expression of ALS-FUS lead to a reduction in NCT and nucleoporin (Nup) density within the nuclear membrane of human neurons. FUS and Nups were found to interact independently of RNA in cells, and to alter the phase separation properties of each other *in vitro*. FUS-Nup interactions were not localized to nuclear pores, but were enriched in the nucleus of control neurons versus the cytoplasm of mutant neurons. Our data indicate the effect of ALS-linked mutations on the cytoplasmic mislocalization of FUS, rather than on the physiochemical properties of the protein itself, underlie our reported NCT defects. An aberrant interaction between mutant FUS and Nups is underscored by studies in *Drosophila*, where reduced Nup expression rescued multiple toxic FUS-induced phenotypes, including abnormal nuclear membrane morphology in neurons.

INTRODUCTION

Nucleocytoplasmic transport (NCT) refers to the active transfer of macromolecules through nuclear pore complexes (NPC) embedded within the nuclear membrane. Each NPC is comprised of multiple copies of 30 different nuclear pore proteins called nucleoporins (Nups). Some Nups contain low-complexity domains with phenylalanine (F)/glycine (G) motifs that undergo phase separation[1], a process whereby macromolecules demix from aqueous solution and form assemblies through weak, non-covalent interactions[2]. Phase separation of F/G-Nups into polymers and hydrogels may contribute to the selectivity filter of the NPC, as the central channel of the pore is enriched with F/G motifs that directly bind and guide nuclear transport receptor-bound cargo through the pore[3].

NCT becomes compromised as a function of aging, particularly in post-mitotic cells such as neurons[4,5]. In dividing cells, the nuclear membrane and NPC disassemble during mitosis, allowing for pore components to turnover and become replenished as needed before pore reassembly[6]. Conversely, in terminally differentiated cells, Nups represent some of the longest-lived proteins and are therefore vulnerable to age- and stress-induced damage[7]. For example, age-dependent changes in nuclear transport receptor expression correlate with nuclear pore deterioration and pore “leakiness”[5]. Further, certain Nups are highly susceptible to oxidative damage and stress-induced degradation in aged and stressed cells, which can lead to further NCT dysfunction[4,8].

The NCT pathway has also been implicated in age-dependent neurodegenerative disorders[4]. Notably, the NCT pathway recently emerged as a therapeutic target in amyotrophic lateral sclerosis (ALS) and frontotemporal dementia (FTD), two related and incurable disorders[9]. In the context of ALS/FTD caused by repeat expansions in *C9orf72*, a series of unbiased genetic screens identified components of the NCT pathway as modifiers of *C9orf72*-induced toxicity[10–13]. Nuclear membrane abnormalities and loss of nucleocytoplasmic compartmentalization were subsequently observed in human *C9orf72* iPSC-derived neurons[11,12,14]. Similar observations were reported in neurons expressing

ALS-linked variants of TDP-43[15] and of profilin 1[16]. Despite an emerging role of NCT in neurodegenerative disease pathogenesis, the mechanism(s) by which NCT-related defects arise in these disorders remain unclear[9].

Herein, we examined the NCT pathway in models of disease-linked fused in sarcoma (FUS). FUS is an ALS/FTD-associated, RNA/DNA binding protein that undergoes nucleocytoplasmic shuttling for various cellular functions[17]. However, nuclear import of FUS is impaired when the nuclear localization sequence (NLS) is mutated in ALS, which abrogates binding between FUS and the nuclear transport receptor karyopherin-β/transportin-1[18]. As a result, mutant FUS accumulates in the cytoplasm where it is thought to exert a toxic gain of function that leads to ALS[17]. Cytoplasmic accumulation of pathological proteins has been shown to correlate with NCT dysfunction, potentially through sequestration of transport factors by pathological proteins[19]. In light of these observations, we investigated the NCT pathway in models of disease-linked FUS. We demonstrate loss of nuclear pore integrity and other phenotypes related to disrupted nucleocytoplasmic transport in multiple systems including isogenic human neurons and *Drosophila* models of FUS-induced toxicity. Interactions between FUS and Nups may underlie these phenotypes, as FUS interacts directly with Nups in cells and *in vitro*, where FUS and Nups alter the phase separation properties of each other. Importantly, reduced expression of Nups mitigates FUS toxicity *in vivo*. Our results indicate that NCT dysfunction is a feature of ALS-FUS, and that targeting aberrant FUS/Nup interactions may be a viable therapeutic strategy for FUS-mediated neurodegeneration.

RESULTS

Nucleocytoplasmic transport is impaired in human neurons expressing ALS-linked FUS.

Impaired NCT has been reported in multiple age-related neurodegenerative disorders[9]. To assess NCT in ALS-FUS iPSC-derived neurons, we examined the distribution of the Ras-related nuclear protein (Ran) between the nucleus and the cytoplasm, referred to as the Ran gradient, which establishes the directionality of normal NCT[9,20]. Normally, Ran is localized in the nucleus, but changes to this gradient are often accompanied by compromised NCT[9,21]. Human induced pluripotent stem cells (iPSCs) harboring the autosomal dominant ALS-FUS mutations, M511Nfs or R521G, were subjected to a protocol for motor neuron differentiation and processed for Ran immunofluorescence analysis (Figure S1). The FUS nuclear localization sequence (NLS) is abrogated by the M511Nfs mutation, leading to severe cytoplasmic mislocalization of the protein in cells and juvenile ALS-onset in humans. Mutations at residue R521 are the most common cause of adult-onset ALS-FUS[22] and also disrupt the FUS NLS albeit to a lesser degree than M511Nfs (Figure S1). We observed a significant decrease in the nuclear-cytoplasmic (N/C) distribution of Ran in iPSC-derived motor neurons harboring the more severe M511Nfs mutation compared to motor neurons derived from control or R521G iPSCs (Figures 1a–1c). We repeated this analysis on motor neurons derived from iPSCs that were gene-edited to correct the M511Nfs mutation (referred as M511Nfs*Cor) compared to isogenic mutant neurons[23]. Again, the Ran N/C ratio was significantly lower in FUS M511Nfs neurons compared to FUS M511Nfs*Cor neurons in both ISL1/2-positive (Figures 1d and 1e) and -negative neurons (Figure 1f). A

Western blot analysis revealed similar levels of Ran protein between FUS M511Nfs and M511Nfs*Cor neurons, suggesting the N/C change was due to a shift in the Ran gradient rather than altered protein levels (Figures 1g and 1h). Similarly, the Ran N/C ratio was significantly lower in FUS R495X neurons compared to the corresponding isogenic control (Figures S2 and S3). Therefore, expression of ALS-FUS is sufficient to disrupt the N/C Ran distribution in ALS patient-derived neurons, leading to higher levels of Ran in the cytoplasm.

Next, we assessed nuclear pore density within FUS M511Nfs and control neurons. In general, neurons exhibited variable nuclear morphologies and degrees of membrane invaginations when fixed. To facilitate immunofluorescence analysis of nuclear pores, neurons were semi-permeabilized prior to fixation, resulting in isolated and intact nuclei that were devoid of membrane invaginations[24]. Neuronal nuclei were probed for nucleoporins (Nups), including the nuclear pore membrane protein 121 kDa (Pom121), a scaffold Nup and Nup62, a central channel Nup. Staining of control nuclei with both markers produced a robust and continuous ring of signal at the nuclear membrane. In contrast, there were numerous gaps in Pom121 and Nup62 signals around FUS M511Nfs nuclei (Figure 2a). This phenotype was quantified using a “cluster analysis” as illustrated in Figure 2b. Briefly, a continuous Nup distribution was assigned a cluster of one (i.e., no gaps). Gaps in nuclear pore signal resulted in a higher cluster number, reflecting a loss of continuous pore signal at nuclear membrane, but not necessarily a clumping of pores. FUS M511Nfs nuclei exhibited significantly more gaps (i.e., higher cluster numbers) for both markers compared to control nuclei (Figures 2c and 2d), although Pom121 and Nup62 did not always co-localize (Figure S4a). Nuclei probed for either marker were binned according to their cluster number in Figures 2e and 2f, confirming that a higher percentage of FUS M511Nfs nuclei exhibited more gaps in nuclear pore signal compared to control nuclei, and vice versa. This analysis could not accommodate additional markers, such as ISL1/2, for co-staining. In a Western blot analysis, total Nup protein levels were similar in mutant and control neurons (Figure S4b and S4c), although we cannot exclude the possibility of reduced Nup expression in a subset of cells with high cluster numbers.

Proper Ran and nuclear pore distributions are required for efficient NCT[20], raising the possibility that transport is also impaired by expression of ALS-FUS. To assess active transport, cultured neurons were transduced with a lentiviral construct encoding the fluorescent shuttling reporter, tdTomato, fused to a classical nuclear localization sequence (NLS) and nuclear export sequence (NES) at the N- and C- terminus, respectively. We previously showed that nucleocytoplasmic shuttling of this reporter is dependent on nuclear pore activity in neurons[25]. Here, NLS-tdTomato-NES exhibited a diffuse expression pattern and was predominately localized to the nuclei of human neurons (Figure S5a). Fluorescence recovery after photobleaching (FRAP) was performed on nuclear tdTomato fluorescence signal. TdTomato fluorescence was bleached within the entire area of the nucleus, and the then recovery of this fluorescence signal was monitored over a time course of 450 seconds (Figure S5b). Recovery of nuclear tdTomato fluorescence is therefore dependent on nuclear import of the tdTomato reporter from the cytoplasm. Complete nuclear fluorescence recovery was not observed in any FRAP experiment herein, likely because most of the reporter is expressed in the nucleus to begin with and eventually the entire cell becomes

photobleached during the analysis (Figure S5a,b). Nonetheless, the overall tdTomato fluorescence recovery was significantly less efficient in FUS M511Nfs neurons compared to control neurons (Figure 2g) as demonstrated by the area under the recovery curve (Figures 2h). Further, the initial rates of the fluorescence recovery were significantly slower in mutant versus control neurons (Figure 2i). The reduced FRAP recovery in mutant neurons is not due to differential expression of the NLS-tdTomato-NES protein between lines (Figure S5c).

As nuclear export may also contribute to diminished NCT, tdTomato fluorescence was measured in the cytoplasm of the same neurons that underwent nuclear photobleaching. Nuclear export of photobleached tdTomato molecules effectively dilutes cytoplasmic tdTomato fluorescence, thereby diminishing cytoplasmic tdTomato fluorescence over time (Figure S5b). However, cytoplasmic tdTomato fluorescence did not decrease in mutant neurons, indicative of an export defect, to the same extent as in control neurons (Figure S5d). While differences in nuclear import and export were observed between aged (DIV 56–60) mutant FUS and control neurons, no differences were detected between young (DIV 18) mutant and control neurons (Figures S5e–h), suggesting the effect of mutant FUS on NCT may manifest with age, consistent with recent observations in ALS-C9orf72 human neurons[14].

FUS directly interacts with nucleoporins in cells and *in vitro*.

To gain insight into how mutant FUS disrupts NCT, we explored the possibility that FUS interacts directly with nuclear pore proteins. We considered proteins that were immunoprecipitated by FUS from HEK-293T cells and subsequently detected by a mass spectrometry (MS) analysis[26]. While most of the FUS-interacting proteins were other RNA-binding proteins, several nuclear pore associated proteins were detected, albeit in low abundance. We pursued Nup62 given the important role of this protein in NCT and prior reports that Nup62 becomes dysregulated in models of neurodegeneration[9,27]. This interaction was validated here through IP of both FUS and Nup62 in multiple ALS-FUS iPSC lines, including FUS P525L and an isogenic control[28] (Figure 3a), and additional mutant FUS and control lines (Figure S6). The IP was performed with and without RNase, which was added when the lysates were applied to the antibody-bound beads (illustrated in Figure S6a). As opposed to RNA-dependent interactions of FUS[26,29], the FUS/Nup62 interaction was enhanced in the presence of RNAse (Figures 3b,c and Figure S6). RNase treatment likely removed RNA-dependent protein interactions of FUS in the IP reaction, thus increasing the opportunity for Nup62 to bind FUS (Figure S6a).

To expand on these findings, full-length FUS WT, full-length ALS-FUS M511Nfs and full-length Nup62 were recombinantly expressed and purified *in vitro* as fusion proteins containing an N-terminal maltose binding protein (MBP) solubility tag[30] (Figure S7a). Due to the extreme aggregation propensity of recombinant Nup62 after liberation from the MBP tag, we elected to analyze the biochemical interaction of FUS and Nup62 while fused to MBP. Co-IP of MBP-FUS with MBP-Nup62 confirmed that these proteins directly and specifically interact even in the presence of the MBP tags (Figure S7b).

FUS and Nup62 alter the phase separation properties of each other.

In light of the functional implications of phase separation for both FUS[2] and Nup62[3], we also considered whether one protein could affect the phase separation properties of the other. First, the phase separation of each protein alone was initiated with polyethylene glycol (PEG), a molecular crowding reagent. To monitor the phase separation of each protein using fluorescence microscopy, full-length MBP-FUS and full-length MBP-Nup62 were doped with Alexa-555 labelled MBP-FUS and Alexa-488 labelled MBP-Nup62, respectively. In the presence of PEG, MBP-FUS readily condensed into dynamic spherical droplets (Figure 4a, Figure S8, Supplemental Video 1), similar to prior reports [30–32]. Under these conditions and over a 24-hour timeframe, there were no discernable differences in droplet formation or droplet morphology between MBP-FUS WT and MBP-FUS M511Nfs (Figure 4a and Figure S9), indicating that mutation of the FUS NLS does not affect the physicochemical properties of the protein with respect to droplet formation. In contrast to MBP-FUS, MBP-Nup62 assembled into non-spherical particles in the presence of PEG (Figure 4a). Neither MBP-FUS droplets nor MBP-Nup62 assemblies were formed under these conditions in the absence of PEG (Figure S10).

Next, we investigated whether MBP-Nup62 affects the phase separation of MBP-FUS and vice versa, by mixing MBP-FUS (either WT or M511Nfs) with MBP-Nup62. After combining equimolar amounts of the proteins, PEG was added to the mixture and droplet formation was monitored by fluorescence microscopy. Strikingly, MBP-FUS WT (Figure 4a) formed irregular shaped or amorphous assemblies *in lieu* of spherical liquid droplets when MBP-Nup62 was added to the mixture. Further, the appearance of MBP-Nup62 amorphous assemblies was accelerated and augmented by the presence of FUS (compare MBP-Nup62 alone to MBP-Nup62 + MBP-FUS at every time point in Figure 4a). Compared to the droplets formed by MBP-FUS, FRAP measurements of FUS/Nup amorphous assemblies appeared less dynamic with lower fluorescence recovery. However, these species tended to oscillate in solution (Supplemental Video 2), contributing to the variability of the FRAP recovery curves (Figure S8). Collectively, these results demonstrate a synergistic effect of Nup62 and FUS on the phase separation properties of the other, where co-mixing leads to non-spherical, less dynamic and less liquid-like species. These effects were specific for sequences encoded by FUS and Nup62, as addition of free MBP protein had no discernable effect on FUS (Figure S11a) or Nup62 (Figure S11b) condensation, although free MBP did co-localize with MBP-FUS droplets as reported[33]. Results of the co-mixing reactions were the same, regardless of whether FUS WT (Figure 4a) or FUS M511Nfs (Figure S9) was mixed with Nup62. Apparently, NLS mutations in FUS do not alter the Fus/Nup interaction *in vitro*. We note that TEV-proteolytic cleavage of the MBP-tag also induced FUS droplet formation as reported[30], but we noticed that the TEV enzyme itself aggregated over time and was therefore viewed as a confounding factor for our co-mixing studies of MBP-FUS and MBP-Nup62.

Given that FUS and Nup co-IPs were enhanced in the presence of RNase (Figures 3 and S6), we performed the same co-mixing experiments in the presence of torula yeast RNA at a mass ratio of RNA:FUS:Nup62 ≈ 1.5:1:1. Strikingly, the presence of RNA prevented the formation of irregular shaped FUS/Nup assemblies. Instead, FUS condensed into spherical

species, even though Nup62 was present (Figure 4b). Further, some Nup signal co-localized within FUS droplets, suggesting the FUS/Nup interaction was not fully abrogated by RNA but rather might be occurring in the droplet phase (Figure 4b). Thus, RNA modulates FUS/Nup62 interactions.

Cytoplasmic interactions between nucleoporins and FUS are enhanced in mutant FUS neurons.

While the co-IP studies and droplet assays did not demonstrate differential interaction between Nup62 and mutant versus wild-type FUS (Figures 3, S6 and S7), the nature of FUS/Nup interactions could depend on their localization within the cell. Immunofluorescence analyses demonstrated that wild-type FUS is predominately localized in the nucleus of cells whereas ALS-linked mutations in the NLS of FUS cause cytoplasmic mislocalization of the protein (Figures S1–S3 and 5a). However, there is no compartmentalization of cytoplasmic and nuclear-specific factors in the biochemical assays. Therefore, we investigated the FUS/Nup interaction *in situ*. Given that Nup62 is a F/G-Nup, and that FUS may generally interact with this class of proteins, we performed co-immunofluorescence analysis with an anti-F/G-Nup monoclonal antibody (mAb414)[15,16] together with an anti-FUS antibody. Some mAb414 signal was also detected in the nucleus and the cytoplasm, the latter which may represent F/G-Nups associated with annulate lamellae (Figure 5a)[6,34–36].

The proximity ligation assay (PLA) was employed using the same FUS and mAb414 antibodies. The PLA generates a signal when two proteins are proximally located within ~40 nm of each other and thus reports on potential protein-interactions *in situ*. PLA signal was detected between FUS and F/G Nup proteins in both control and mutant neurons. *A priori*, we expected PLA signal at the nuclear membrane where the pore signal was diminished. However, PLA signal was not localized to the membrane, and was strikingly different between genotypes (Figure 5b). For control neurons, prominent FUS/mAb414 PLA signal was detected within nuclei, whereas the PLA signal was distributed between the nucleus and the cytoplasm of mutant neurons (Figure 5b). Quantification of total FUS/mAb414 PLA signal was significantly higher in M511Nfs neurons (Figure 5c), which could be due to higher endogenous FUS expression in mutant cells (Figure 3a and[23,37]). Equatorial planes of each cell were used to quantify the cytoplasmic-nuclear (C/N) ratio for FUS/mAb414 PLA signal (Figure 5d), which was significantly shifted toward the cytoplasm in mutant neurons compared to control (Figure 5e).

In addition to the pan F/G Nup mAb414 antibody, we also performed the PLA for FUS and individual F/G Nup proteins, including central channel Nups (Nup62 and Nup98) and a nuclear basket Nup (Nup153). Total PLA signals for these other Nups were lower than mAb414 and did not differ significantly between genotypes (Figures S12e, S12h and S12k). However, all three Nups produced a significantly higher C/N PLA ratio in FUS M511Nfs neurons (Figures 5f, 5g and 5h). Plotting PLA intensities in grey values revealed that the nuclear PLA signal was reduced in the mutant neurons relative to the control neurons for all Nup antibodies tested, although this did not reach statistical significance for the FUS/mAb414 PLA (Figures S12a, S12c, S12f and S12i). Further, there was a significant increase

in cytoplasmic FUS/Nup PLA signal in the mutant neurons compared to the control for all Nups except Nup98 (Figures S12b, S12d, S12g and S12j). Taken together, these data indicate that enhanced FUS/Nup interactions within the cytoplasm of ALS-FUS neurons is largely due to a shift in signal from the nucleus to the cytoplasm.

PLA was then used to detect potential interactions between nuclear pore proteins themselves using mAb414 and anti-Nup62 antibodies (Figure 5i). While the total PLA signal was not significantly different between genotypes (Figure S12n), there was a significant increase in the C/N ratio for the Nup62/mAb414 PLA in mutant compared to control neurons (Figure 5j). This result is consistent with a displacement of nuclear pore proteins from the nucleus and/or the nuclear pore complex in mutant FUS neurons (Figures S12l and S12m).

Nuclear abnormalities associated with ALS-linked FUS are rescued by knock-down of Nup62 *in vivo*

Our data suggests that interactions between ALS-linked FUS variants and nucleoporins could become pathological, and manifest in disease-relevant phenotypes within neurons. We therefore examined the effect of nucleoporin expression on FUS-induced toxicity in *Drosophila*[38,39]. Targeted overexpression of FUS WT and disease-causing variants (R518K and R521C) in fly eyes caused significant eye degeneration characterized by depigmentation, ommatidial fusion and resultant waxy external eye phenotype (Figure S13a). Overexpression of Nup62 in this context exacerbated the eye degeneration in WT and mutant FUS flies (Figure S13a), whereas Nup62 overexpression on its own was well tolerated (Figure S13b) thus confirming the increased toxicity is not due to combined individual toxicities. In contrast, knocking down Nup62 using an RNAi line in FUS WT and mutant flies significantly rescued FUS-mediated eye degeneration (Figures S13a,c). In addition to Nup62, knocking down other nucleoporins including Nup54, Nup98 and Nup214 also rescued FUS toxicity (Figures S13–S15). RNAi-mediated knockdown of Nup37, Nup43, Nup153 and Nup205 in flies exhibited a partial rescue of the eye degeneration phenotype induced by FUS overexpression (Figure S15). These data illuminate multiple FUS/Nup interactions that influence cellular homeostasis *in vivo*.

We investigated whether reducing nucleoporin levels could also rescue FUS-induced defects in cell types that are relevant to ALS. To this end, we used previously published fly lines that overexpress RFP-tagged FUS-WT and mutant FUS-P525L[40] in ventral nerve chord (VNC) neurons (Figure 6a). FUS P525L is an ALS-linked variant that also results in the eye-degeneration phenotype, which is partially rescued with Nup62 RNAi (Figure S16a). FUS WT distributes primarily into punctate structures within the nucleus (Figure 6a, top). In contrast, FUS P525L exhibits a granular expression pattern, distributed between the nucleus and cytoplasm (Figure 6a, bottom). Due to a lack of antibodies available for *Drosophila* Nup62, we were unable to determine Nup62 subcellular distribution. VNC neurons were stained with Lamin C to assess nuclear morphology (Figure 6a), revealing significantly more FUS-P525L-expressing neurons with nuclear invaginations compared to FUS WT (Figure 6b). Nuclear invaginations appear as wrinkled membranes and are indicative of membrane disruptions[10]. Again, Nup62 knockdown significantly ameliorated the nuclear morphology defects caused by FUS-P525L expression (Figure 6b). The protective effect

of Nup62 knock-down is not caused by changes in FUS expression or localization, as the nuclear levels and the nucleo-cytoplasmic (N/C) ratio of FUS-P525L was unchanged upon Nup62 knockdown (Figures 6c and 6d). Further, Nup62 knockdown did not affect FUS-P525L puncta (Figures S16b, c), which may represent RNA granules or complexes of a non-pathological nature.

Finally, we probed for nuclear morphology abnormalities in post-mortem human ALS-FUS cases with either the H517Q or R521C mutation (Supplemental Table 1). Immunohistochemistry (IHC) of these ALS-FUS cases showed instances of abnormal nuclear morphology associated with cytoplasmic FUS inclusions. In contrast to the round shape of a control nucleus containing nuclear FUS signal (brown), some mutant FUS nuclei deviated from a round or circular shape. These neurons also exhibited cytoplasmic mislocalization of FUS (Figure 6e, top panel). To better visualize this, immunofluorescence for FUS with DAPI counterstain was analyzed using confocal microscopy, which further resolved the unusually misshapen nuclear morphology in FUS inclusion-bearing cells (Figure 6e, bottom panel). In a separate IHC analysis, we probed the FUS R521C case, which contains pathological FUS inclusions[41] for Nup62. Obvious Nup62 inclusions were not detected in this case. Although this case also showed some lower motor neurons with misshapen nuclear Nup62 staining, at least a few similar cells were seen in the normal controls (Figure S17). Taken together, nuclear abnormalities appear to be a feature of FUS-mediated ALS, a phenotype that is attenuated by targeting Nup62 expression.

Modulation of Nup62 expression rescues FUS-induced toxicity *in vivo*.

Using the above *Drosophila* models of FUS-induced toxicity, we assessed whether knockdown of Nup62 in fly neurons could also provide a survival benefit. The RFP-tagged FUS animals did not survive to the stage of eclosion. To circumvent this issue, a pan-neuronal conditional expression driver (ElavGS-gal4) was used to induce transgene expression in Day-1 adults. Indeed, Nup62 RNAi significantly improved the survival of both WT and P525L-expressing flies (Figure S18). In contrast to the RFP-tagged FUS animals, *Drosophila* models of FUS WT, R518K and R521C constitutively expressing FUS under a motor neuron driver survived to adulthood, albeit with shortened survival compared to non-transgenic animals. Animals expressing ALS-linked FUS variants exhibit shortened survival curves compared to FUS WT animals (Figure 7a–d), particularly in the case of FUS R521C mutant animals. While Nup62 RNAi significantly improved survival in all fly lines, the protective effect of Nup62 knockdown was most pronounced in FUS R521C flies (Figure 7c). Further, mutant FUS animals exhibit crumpled wing morphologies, which may reflect locomotor dysfunction during eclosion[42]. This phenotype was also ameliorated with Nup62 RNAi (Figure 7e). Collectively, our data demonstrate a synergistically toxic interaction between mutant FUS and Nup62 *in vivo*.

DISCUSSION

Emerging evidence indicates that the NCT pathway may play a global role in neurodegenerative disease, having been implicated in Alzheimer's disease, FTD, ALS, Huntington's disease, and others[4,9–11,15,16,27]. Across multiple model systems for these

disorders, defects in the NCT pathway can manifest as aberrant nucleocytoplasmic compartmentalization of transport factors, “leaky pores”, impaired NCT, reduced NPC density, and irregular nuclear envelope morphology[9]. Here, we uncovered NCT-related phenotypes in models of ALS-linked FUS. Of note, the reduction in Ran N/C ratio observed here for FUS M511Nfs neurons is comparable to the decrease reported for ALS-C9orf72 human neurons[11]. In the case of mutant FUS, the magnitude of the NCT-related defect may correlate with disease severity in human ALS. For example, the Ran gradient was disrupted in neurons expressing FUS M511Nfs or R495X, variants that cause early onset and aggressive disease in humans, but not in neurons expressing FUS R521G[22,23]. As our studies were carried out on a laboratory time frame with endogenous FUS expression, certain phenotypes may not be manifest for moderate variants but could become detrimental with age and *in vivo*.

While NCT abnormalities have been associated with multiple forms of ALS, the underlying mechanism(s) remain ambiguous[9]. Dipeptide repeat sequences derived from C9orf72 directly associated with nucleoporins *in vitro* and appeared to “clog” nuclear pores[43]. However, direct obstruction of NCT by these peptides was not recapitulated in cell culture assays, including in iPSC-derived motor neurons[44]. Our data also do not support direct obstruction of NPCs by mutant FUS. Results of our PLA between FUS and various Nups revealed interaction signals in the nucleus and the cytoplasm, but not localized to the nuclear membrane where NPCs reside. In fact, the localization of the PLA signals was strikingly different between mutant and control neurons, implicating cytoplasmic interactions between mutant FUS and Nups in our observed NCT-related defects (Figure S19).

In contrast to most interactions of FUS[26,29], FUS and Nup interact directly and more strongly in the absence of RNA. Relatively high levels of RNA in the nucleus favor liquid droplet formation of various RNA binding proteins, including FUS. Conversely, RBPs exhibit poor solubility in cellular environments with low RNA concentrations, such as the cytoplasm[32,45]. Here, FUS liquid droplet formation was perturbed by Nup62, leading to the formation amorphous assemblies. In this regard, the effects of Nup62 on FUS contrast starkly with the solubilizing effects of nuclear transport receptor karyopherin-β[9]. Further, RNA inhibited the formation of FUS/Nup62 amorphous assemblies. These data support a model whereby FUS and FUS/Nup complexes are in the soluble, liquid phase within the nucleus, but enter a less dynamic (e.g., gel-like) phase in the cytoplasm. This model explains how FUS variants can differentially interact with Nups *in situ*, but not necessarily *in vitro* (Figure S19). For isolated proteins, the effects of Nup62 on the phase separation of FUS, and vice versa, were indistinguishable between WT and ALS-linked FUS. Consistent with a report of other NLS-FUS variants, the LLPS behavior of isolated WT and FUS M511Nfs were the same in our studies[31]. Collectively, these data indicate the mislocalization of mutant FUS into the cytoplasm, an environment with relatively low RNA levels, rather than a physiochemical property of the mutant protein itself accounts for the differential interaction of mutant FUS and Nups compared to FUS WT (Figure S19).

Aberrant mutant FUS/Nup interactions may underlie the observed NCT-related defects in our human neurons. Upregulated FUS expression in mutant FUS human neurons may exacerbate the formation of mutant FUS/Nup cytoplasmic complexes[23]. Expression

of mutant FUS also led to enhanced cytoplasmic localization of the Nup proteins, as determined by our PLA. Interactions between FUS and Nup62 have the potential to form amorphous assemblies reminiscent of insoluble oligomers or small aggregates. Despite being long-lived, Nups are robustly synthesized proteins, a fraction of which remain in the cytoplasm until their insertion into NPCs by a piecemeal mechanism in post-mitotic cells[7]. Insoluble cytoplasmic FUS/Nup62 complexes could physically trap Nup62 and other Nups in the cytoplasm (Figure S19). These species could also be targeted by the proteasome thereby prohibiting proper Nup assembly into NPCs. Diminished nuclear pore signal in our ALS-FUS neurons may account for the reduced nucleocytoplasmic transport capacity in these cells. Indeed, a recent study demonstrated that overexpression of POM121 restored normal expression of certain nucleoporins, which in turn ameliorated NCT defects in ALS-C9orf72 human neurons[14]. Therefore, it seems logical that the number of functional NPCs would correlate with nucleocytoplasmic capacity.

The toxic nature of the mutant FUS/Nup interaction is underscored by results from *Drosophila* models of acute FUS toxicity. While overexpression of FUS is toxic, overexpression of Nups exacerbated this toxicity, possibly by driving the formation of toxic FUS/Nup complexes (Figure S19). Further, over-expressed ALS-linked FUS in fly motor neurons caused more severe phenotypes than FUS WT (e.g., higher incidence of both nuclear membrane distortions and crumpled wings, as well as shortened survival). In all experiments, knock-down of Nups attenuated toxic FUS-mediated phenotypes *in vivo*. We speculate that FUS/Nup interactions may become toxic *in vivo* in acute models of toxicity because endogenous levels of RNA cannot mitigate aberrant FUS/Nup phase transitions (Figure 4). It follows that knocking down one of the toxic interaction partners (e.g., Nups) reduces the opportunities for FUS/Nup complexes to form, thereby attenuating toxic FUS-mediated phenotypes in animals.

We cannot exclude indirect contributions of mutant FUS NCT decline. For instance, mutant FUS has been shown to activate stress-response pathways[23,46]. Nuclear pore integrity and the nucleocytoplasmic distribution of transport factors are affected by elevated levels of cellular stress, including reactive oxygen species and excitotoxicity[8,47]. The results of our PLA data also reveal interactions between FUS and Nups in the nucleus of control cells. Given that both FUS and Nups are involved in nuclear functions unrelated to NCT, such as DNA repair and transcription[17,48], we speculate that normal biological functions could rely on nuclear FUS/Nup interactions. By extension, reduced FUS/Nup interactions in the nucleus could contribute to NCT-related defects through a loss-of-function mechanism. FUS WT/Nup interactions warrant further investigation, also in light of our results showing that knock-down of Nups attenuates toxicity induced by FUS WT overexpression in flies.

Selective inhibitors of exportin-1 (SINE) are currently being tested in humans with ALS. While these inhibitors modulate nuclear export, thus preventing aberrant misexpression of proteins in the cytoplasm, they may also exert therapeutic effects through other mechanisms[49]. Interestingly, genetic downregulation of exportin-1 was neuroprotective in a *Drosophila* model of FUS overexpression[50], consistent with our results showing protective effects of Nup knockdown in two different FUS *Drosophila* models. Taken together, our

results implicate impaired NCT in FUS-mediated ALS and support the NCT pathway as a viable therapeutic target for multiple causes of neurodegeneration.

MATERIALS AND METHODS

Additional methods details can be found in the accompanying Life Sciences Reporting Summary.

iPSC culture, characterization and spinal motor neuron differentiation

iPSC culture maintenance, characterization and differentiation were performed as previously described in[23]. Before differentiation, iPSCs were confirmed pluripotent by immunofluorescence analysis with OCT4 and SOX2 pluripotency markers as described on our previous report[23] (Figure S2a). In brief, an embryoid body based small molecule approach[51] was adapted to differentiate iPSCs to spinal motor neurons, consistently yielding around 40% of ISL1/2 positive motor neurons (Figure S1b). Neuron cultures were maintained in motor neuron medium for 6–8 weeks (unless stated otherwise) and media was half-changed every 3–4 day. Cultures were treated with 1 μM AraC (Sigma, C6645) to eliminate dividing progenitors at DIV 4. A detailed description of the media components and differentiation protocol used here has been described by us previously[23].

iPS cell engineering of FUS R495X lines

The FUS R495X line and isogenic control lines were generated as follows. Euploid (46;XY) KOLF2.1 iPS cell line was derived from KOLF2-C1 cells[52] in which a 19 base pair deletion in exon 5 of ARID2 was repaired by gene editing. The culture and editing of KOLF2.1 cells was performed essentially as described[52]. The FUS R495X single nucleotide variant (C>T) was generated using a guide RNA that overlaps codon 495 of FUS and a 100-nt single-stranded oligonucleotide (ssODN) donor template. Briefly, pre-assembled Cas9 RNP (2 μg IDT HiFi V3 Cas9 and 1.6 μg Synthego synthetic modified sgRNA) and 200 pmol ssODN (Alt-R™ HDR Ultramer; IDT) were added to 20 μl P3 buffer containing 1.6 × 10^5 Accutase dissociated iPSCs and nucleofected in a 16-well Amaxa 4D cuvette (Lonza; Primary Cell P3, pulse code ‘CA137). Cells were cultured for three days under cold shock conditions (32°C/5%CO_2) and in the presence of Revitacell (1X; ThermoFisher) and HDR enhancer (30 μM; IDT) for the first 24 and 48 hrs, respectively. Upon reaching confluence, cells were dissociated and plated at low density to obtain single cell-derived clones. Clones were screened by Sanger sequencing of PCR amplicons to identify the desired homology-directed repair events in FUS.

PCR primer (forward): 5’- GGGAACATAGGGGAATGGGAATATG. PCR primer (reverse): 5’- TGGTCACTTTTAATGGGAACCAGAG.

Sanger sequencing primer (forward): 5’- TCTTTTGTCCTAGGGGGTAAC. Sanger sequencing primer (reverse): 5’- TCCACCTAGCCCTCAAAATG

Immunofluorescence microscopy for iPSC-derived neurons

Cells plated on the coverslips were fixed with 4% paraformaldehyde (Fisher Scientific, AAA1131336) for 15 min and permeabilized with 1% Triton X-100 (Sigma, T9284)

for 10 min at room temperature. Coverslips were blocked with PBSAT buffer (1% BSA and 0.5% Triton X-100 in PBS) for 1 hour and probed with primary antibodies as follows: 1:1000 mouse anti-OCT4 (R&D Systems, MAB17591-SP)[23]; 1:1000 mouse anti-SOX2 (R&D Systems, MAB2018-SP)[23]; 1:200 rabbit anti-Ran (Bethyl Laboratories, A304-297A)[16]; 1:500 rabbit anti-FUS (Proteintech, 11570-1-AP) [23]; 1:500 mouse anti-Islet 1,2 (Development Studies Hybridoma Bank, 39.4D5)[23]; 1:400 rat anti-Nup62 (Abcam, ab188413)[47]; 1:200 rabbit anti-Pom121 (Proteintech, 15645-1-AP)[16]; 1:2000 mouse anti-mAb414 (Abcam, ab24609)[16,57]; 1:200 rat anti-Nup98 (Abcam, ab50610)[14,57]; 1:200 mouse anti-Nup153 (Abcam, ab24700)[8]. After washing, secondary antibodies were diluted at 1:2000 and incubated for 1 hour at room temperature as described[53]. Conjugated Alexa Fluor-647 anti-Tuj1 antibody (BioLegend, 657405)[23] at 1:400 dilution was used followed by secondary antibody incubations. Cells were counterstained with DAPI and coverslips were mounted with ProLong Gold anti-fade reagent (Invitrogen, P36930).

Image acquisition and processing for iPSC-derived neurons

All fluorescence signals for iPSC-derived neurons were imaged with a Leica DMI 6000 inverted fluorescent microscope equipped with APO 63X/ 1.4 NA oil immersion lens and a filter set for fluorophores in Cy3, Cy5, GFP, and DAPI channels (center/ band width, nm: EX 545/39, 620/60, 470/40, 360/40; EM 605/75, 700/75, 525/45, 470/40). Images were collected with Leica DFC365 FX camera (6.45 μm pixel size) using AF6000 Leica Software v3.1.0 (Leica Microsystems). Whole cell, 12-bit stacks images with 0.2 μm step size were acquired (50–70 planes). Immersion oil (Leica, 11513859) with 1.518 refractive index at room temperature was applied to the lens. Coverslips were mounted with ProLong Gold anti-face reagent (Invitrogen, P36930) with a refractive index of 1.46. All images were acquired with identical microscope settings within individual experiments. Brightness and contrast were adjusted equally for all images and cropped insets were generated in the same manner among all the experiments to facilitate visualization of representative cells. For any image adjustment, identical settings were always applied to all cells, irrespective of genotype. Neurons that were clumped, overlapping or obscured by debris were excluded from the quantification.

Image analysis and quantification for iPSC-derived neurons

***Ran nuclear-cytoplasmic ratio analysis*:** After immunostaining, fluorescent signals of the whole cells were collected using z-stacks and the maximum projected images from the center 5 planes were created for nuclear-cytoplasmic Ran ratio analysis. Nuclear and cytoplasmic areas were defined using DAPI and anti-Tuj1 (reactive for class III beta-tubulin) fluorescent signals respectively. Number of cells used for this analysis: pooled controls, n=151; M511Nfs, n=117; R521G, n=63, M511Nfs*Cor, n=103; M511Nfs, n=90 cells. No statistical methods were used to pre-determine sample sizes but our sample sizes are similar to those reported in previous publications[11,16]. Data collection and analysis were not performed blind to the conditions of the experiments.

***Nuclear pore cluster analysis*:** Neurons were semi-permeabilized with ice-cold permeabilization buffer (80 mM PIPES pH 6.8, 5 mM EGTA, 1 mM $MgCl_2$, 0.5% Triton X-100) on ice for 3 min and washed three times with DPBS (Corning, 21-031-CV).

Coverslips were fixed and immunostained as described above. Fluorescent signals of the whole nuclei were collected using z-stacks and the center plane image (with the widest DAPI staining) was exported for the following image processing. Fluorescent signals were thresholded using the same parameter within experiments (differentiations) and binary images were created for cluster analysis using ImageJ software. Numbers of areas represent numbers of clusters. Number of nuclei used for this analysis: M511Nfs*Cor, n=152, M511Nfs, n=144 nuclei. No statistical methods were used to pre-determine sample sizes but our sample sizes are similar to those reported in previous publications[14]. Data collection and analysis were not performed blind to the conditions of the experiments.

***PLA analysis*:** After PLA staining, fluorescent signals of the whole cells were collected using z-stacks and the maximum projected images from the center 10 planes were created for nuclear-cytoplasmic PLA ratio analysis. Nuclear and cytoplasmic areas were defined using DAPI signals and phase contrast respectively. Maximum projected images from the whole cells were created for total PLA intensity measurements. Soma boundaries were defined using phase contrast images. Number of cells used for this analysis: M511Nfs*Cor, n=69; M511Nfs, n=68 cells. No statistical methods were used to pre-determine sample sizes but our sample sizes are similar to those reported in previous publications[54,55]. Data collection and analysis were not performed blind to the conditions of the experiments.

Fluorescence recovery after photobleaching (FRAP)

For FRAP analysis in iPSC-derived neurons, cells plated on coverslips were transduced with high titer lentivirus expressing NLS-tdTomato-NES shuttling reporter at DIV 3 (MOI=5). The tdTomato shuttling reporter construct was a kind gift from Dr. Martin Hetzer (Salk Institute, USA) and re-cloned to a lentiviral vector as described in[25]. Phenol-free neurobasal medium (Invitrogen, 12348-017) was used in motor neuron medium. At DIV 55–60, coverslip was transferred to a 12mm coverslip chamber (Bioscience Tools, CSC-12) and FRAP procedures as previously described[53] were performed. In brief, experiments were carried out on a Leica SP5 II laser scanning confocal microscope using 40× 1.3 NA water immersion objective. For every neuron, one pre-bleached image was collected and tdTomato signals in the whole nucleus were bleached for 10 iterations of 100% 561nm laser power. Recovery of the fluorescence signals was monitored by collecting 150 post-bleached images spaced at 3 sec intervals. The fluorescence intensity was measured by drawing regions of interest in the bleached area (whole nucleus), the whole cell, and in background area without cells at each time point using AF6000 Leica Software. Because the entire field of view including the nucleus and the cell soma are exposed to continuous pulses of light, gradual photobleaching precludes a full FRAP recovery. Datasets were generated in excel and analyzed using easyFRAP-web tool[56] (version 1.8, https://easyfrap.vmnet.upatras.gr). To account for global bleaching during image acquisition, each post-bleached fluorescence intensity was normalized to the fluorescence intensity of an unbleached area at each timepoints. Fluorescence recovery curves were plotted using GraphPad Prism v8.1.2. Each time points represented means ± s.e.m.. Exponential one-phase association curve fitting was used to calculate area under the curve as described[11,16,57]. Approximately 20 neurons were imaged per line per differentiations. Neurons at DIV18-22 and DIV 56–60 were considered as young and old neurons, respectively. Three independent neuron differentiations were

performed. Data collection and analysis were not performed blind to the conditions of the experiments.

For FRAP analysis of co-mixing reactions with recombinant proteins, experiments were carried out on the same scope as above but with a 60x oil objective. One prebleach image was collected and Alexa555 signal in bleach region (~0.7-0.9 μm diameter) was bleached for 8 iterations (1.293 s each) using 561nm laser at 100% intensity. After bleaching, 300 images were acquired every 1.293s. Fluorescence intensity was measured in the bleach region, an unbleached region, and a background region outside droplet/amorphous assembly at each time point using AF6000 Leica Software. Fluorescence recovery curves were generated after correcting for background signal and photofading using a custom Python script based on equations described in easyFRAP-web tool 84 (https://easyfrap.vmnet.upatras.gr). Fluorescence recovery curves were plotted using GraphPad Prism v8.1.2.

Western blotting

Cells were lysed with RIPA buffer (Westnet, BP-115-500) supplemented with fresh protease inhibitors (Roche, 11873580001). Lysates were incubated on ice for 15 min and cleared through centrifugation (16000 g) for 15 min at 4°C. Supernatants were collected and protein concentration were determined using BCA assay kit (Thermo Scientific Pierce, 23227). Western Blotting analysis were performed as described[23]. After blocking, blots were incubated with primary antibodies overnight at 4°C. Primary antibodies were used as follows: mouse anti-FUS (1:200, Santa Cruz, SC-373698; validated in Supplemental Figure 7); rabbit anti-Nup62 (1:1000, Bethyl Laboratories, A304-942A; validated in Supplemental Figure 7); mouse anti-Tuj1 (1:1000, BioLegend, 801201); mouse anti-maltose binding protein (Cell Signalling Technology, 2396; validated in Supplemental Figure 7). Followed by washes, blots were incubated with secondary antibodies as described[23] and visualized using Odyssey Infrared Imager (LiCor, 9120). Image J was used for densitometry measurements. Data collection and analysis were not performed blind to the conditions of the experiments.

Immunoprecipitation

Immunoprecipitation (IP) analysis from cell lysates was performed as previously described[26]. In brief, cells were lysed with IP lysis buffer (1% Triton X100, 50 mM Tris-HCl, 150 mM NaCl, 5 mM EDTA, 10% Glycerol pH 7.5, fresh protease inhibitors) and cleared through centrifugation (16000 g) for 15 min at 4°C. Protein concentration were determined using BCA assay kit (Thermo Scientific Pierce, 23227) and 500 μg- 1 mg of lysates were subjected to IP. Magnetic Dynabeads protein G (Invitrogen, 10003D) were washed and charged with 40 μg rabbit anti-FUS antibody (Genscript, lab made), 3 μg rabbit anti-Nup62 antibody (Bethyl Laboratories, A304-942A) or 3/40 μg Chrompure rabbit IgG whole molecule (Jackson ImmunoResearch, 011-000-003) for 2 hr at 4°C by rotation. Charged beads were washed and 500 μg- 1 mg of lysates were incubated with the charged beads overnight at 4°C by rotation. To test if the interactions were RNA-mediated, lysates along with beads were treated with or without 50 μg/mL RNase A (Invitrogen, 12091021) and incubated at 37°C for additional 30 min after the overnight incubation. Supernatants were discarded and beads were washed three times thoroughly with IP buffer to eliminate

unbound proteins. Beads were boiled at 95°C for 10 min in 1x SDS sample buffer (Westnet, BP-111R) to elute bound proteins. Proteins were subjected to western blotting analysis as described.

IP analysis on recombinant proteins were performed as follows. MBP-Nup62 (150 nM) was mixed with MBP-FUS (75 nM) or MBP (75 nM) and incubated at room temperature for 30min. The protein mixtures were then incubated with protein A magnetic beads (SureBeads, Biorad) pre-charged with anti-Nup62 antibody (Bethyl Laboratories, A304-942A) for 2h. After washes, proteins were eluted by heating the beads in Laemmli buffer at 95°C for 5min and analyzed by Western blot. To assess non-specific binding of FUS to the beads, similar experiment with FUS was performed in the absence of Nup62. Data collection and analysis were not performed blind to the conditions of the experiments.

Proximity ligation assay

In situ protein-protein interactions were detected using Duolink proximity ligation assay (PLA) reagents according to manufacturer's instructions. In brief, cells were fixed with 4% PFA and permeabilized with 1% Triton-X100. Following by blocking with Duolink Blocking Solution (Sigma, DUO82007) for 1 hour at 37°C, cells were incubated with primary antibodies (as described in the Immunofluorescence staining section) diluted with Duolink antibody diluent (Sigma, DUO82008) for 1 hour at room temperature. Duolink PLA secondary probes (anti-rabbit IgG PLUS, DUO92002; anti-mouse IgG MINUS, DUO92004; anti-rat IgG MIUNS probes were generated using Duolink Probemaker kit DUO92101 based on manufacturer's protocol.) were applied to the cells for 1 hour at 37°C. PLA probe hybridization was performed by incubating cells with ligation mix for 30 min at 37°C. Amplification was followed by 100 min, 37°C incubation with polymerase: Texas Red oligonucleotides mix. Components of ligation and amplification were from Duolink In Situ Detection Red kit (DUO92008). Coverslips were mounted with Duolink mounting medium with DAPI (DUO82040). Data collection and analysis were not performed blind to the conditions of the experiments.

Plasmid construction

Plasmid encoding MBP-FUS WT on pTHMT backbone was obtained from Addgene (#98651). All plasmid constructs for recombinant protein expression were constructed onto this vector. Nup62, FUS M511Nfs and MBP DNA sequence were synthesized as gBlocks Gene Fragments (Integrated DNA Technologies) and assembled into vector using NEBuilder HiFi DNA Assembly (New England Biolabs).

Expression and purification of recombinant proteins

All the proteins were expressed in *E.coli* Rosetta (DE3) (Novagen). Bacterial cultures were grown at 37°C until OD=0.4, induced for protein expression with 1 mM IPTG and further grown for 16–18h at 16°C. Cells were harvested by centrifugation and stored frozen at −80°C. Only full-length FUS and Nup62 proteins were used herein.

Frozen cell pellet expressing MBP and MBP-Nup62 were thawed on ice, resuspended and sonicated in ice cold lysis buffer (20 mM sodium phosphate, 300 mM NaCl, 10 mM

imidazole, pH 7.6) supplemented with protease inhibitor (cOmplete, EDTA-free protease inhibitor tablet, Sigma), lysozyme and RNAse A (100 μg/ml). Lysate was clarified by centrifugation at 26,000×g for 30min, 4°C and incubated with Ni-sepharose resin (GE Healthcare) pre-equilibriated with lysis buffer for 2h at 4°C on end-to-end rotor. After washes with lysis buffer containing 40 mM imidazole, the protein was eluted in 20 mM sodium phosphate, 150 mM NaCl, 500 mM imidazole, pH 7.6. Peak fractions were pooled and further purified by size exclusion chromatography using HiLoad 16/600 Superdex 200pg (GE Healthcare) equilibrated with 20 mM Tris/Cl, 150 mM NaCl, pH 7.4 at room temperature. Fractions containing the protein of interest were pooled, concentrated using centrifugal filter (10kDa MWCO, Vivaspin) and stored at −80°C.

MBP-FUS WT and M511Nfs were purified as described in[58]. Cell lysate was prepared by sonication in ice cold lysis buffer (20 mM sodium phosphate, 1 M NaCl, 10 mM imidazole, pH 7.6 supplemented with protease inhibitor (cOmplete, EDTA-free protease inhibitor tablet, Sigma) and lysozyme. Protein was first purified using Ni-sepharose resin (GE Healthcare) pre-equilibrated with lysis buffer by batch/gravity method at room temperature. Peak fractions were pooled and further purified by size exclusion chromatography using HiLoad 16/600 Superdex 200pg (GE Healthcare) equilibrated with 20 mM sodium phosphate, 1 M NaCl, pH 7.4 at room temperature. Fractions containing pure MBP-FUS were pooled, concentrated using centrifugal filter (10 kDa MWCO, Vivaspin) and stored in 25% glycerol, 20mM sodium phosphate, 1 M NaCl, pH 7.4 at −80°C.

Fluorophore labelling of recombinant proteins

MBP-FUS WT and M511Nfs were labelled with Alexa-555 maleimide (ThermoFisher Scientific), MBP-Nup62 with Alexa-488 maleimide (ThermoFisher Scientific) and MBP with Alexa-488 TFP ester (ThermoFisher Scientific) according to manufacturer's instructions. Unreacted dye molecules were removed by two serial buffer exchanges using spin desalting columns (7k MWCO, Zeba, ThermoFisher Scientific).

In vitro phase separation assay

MBP-FUS WT and M511Nfs samples were doped with ≤ 2.5% of the respective Alexa-555 labelled proteins. MBP-Nup62 and MBP samples were doped with ≤ 2.7% and ≤ 1% respectively of the corresponding Alexa-488 labelled proteins. MBP-FUS WT (1.5 μM) or M511Nfs (1.5 μM) was mixed with MBP-Nup62 (1.5 μM) and phase separation was initiated by dilution into buffer containing PEG-8000 (USB corporation).The final composition of the phase separation buffer was 20mM Tris/Cl, 158mM NaCl, 3.6% PEG-8000, 3.45% glycerol, pH 7.4. Samples were deposited on 384-well clear plate (ibidi), sealed with plastic film and shaken at 250 rpm at room temperature.

To assess the effect of RNA on FUS/Nup62 phase separation, torula yeast RNA (0.125 mg/ml) was added before addition of PEG such that mass ratio of RNA:FUS:Nup62 ≈ 1.5:1:1. RNA stock was prepared by dissolving 10mg of torula yeast RNA (Sigma Aldrich) in 1ml of 20mM Tris/Cl, pH 7.4 on ice. After centrifugation at 13,000 rpm, 10min, 4°C and dissolved RNA was buffer exchanged into 20mM Tris/Cl, pH 7.4 using spin desalting columns (7k MWCO, Zeba, ThermoFisher Scientific). RNA concentration was estimated

from absorbance at 260nm measured using Nanodrop spectrophotometer (ThermoFisher Scientific).

Images were acquired under 40X air objective with Leica DFC365 FX camera on Leica DMI 6000 inverted fluorescent microscope using AF6000 Leica Software v3.1.0 (Leica Microsystems). Images of RNA experiments were acquired using Nikon Ti E microscope with a cooled CMOS camera (Andor Zyla). Acquisition settings for each protein was same at each time point in the timecourse experiments. Brightness and contrast were adjusted equally across sample conditions in each channel to facilitate visualization of protein species. Full field of view images are shown in the figures. Images of RNA experiments and insets represent cropped and zoomed images of representative protein species. Data collection and analysis were not performed blind to the conditions of the experiments.

Drosophila stocks and maintenance

Transgenic UAS-FUS WT, R518K and R521C lines were generated by the Pandey lab[39]. The RFP-tagged FUS-WT and FUS-P525L lines were a generous gift from Dr. Jane Wu at Northwestern University. RNAi lines were obtained from Vienna Drosophila Research Center for Nup62 (Stock # 100588 KK), Nup54 (Stock # 103724 KK), Nup98 (Stock # 109279 KK), Nup37 (Stock # 109814 KK), Nup43 (Stock # 33645 GD), Nup153 (Stock # 107750 KK), Nup205 (Stock # 38610 GD) and Nup214 (Stock # 41964 GD). All stocks were maintained on standard dextrose media on a 12-hour light/dark cycle.

Drosophila assays

To assess external eye degeneration, GMR-gal4 driver was used to selectively drive expression in fly eyes at 25°C. Quantification of external eye phenotype of 1-day old female flies was performed as previously published[59]. Data collection and analysis were not performed blind to the conditions of the experiment. No statistical methods were used to pre-determine sample sizes but our sample sizes are similar to those reported in previous publications[10,39,60,61].

To assess nuclear membrane morphology in *Drosophila* VNC neurons, D42-gal4 driver was used to selectively drive expression in motor neurons at 25°C. Third instar larval VNC was dissected out and fixed in 4% paraformaldehyde for 20 minutes at room temperature. For immunofluorescence, fixed VNCs were blocked for 1 hour in blocking buffer (5% normal goat serum in 0.2% PBS-Triton X-100). The tissue was incubated in primary antibody overnight (1:100 Mouse anti-Lamin C, DSHB LC28.26) followed by incubation in secondary antibody for 2 hours at room temperature (1:500 Goat anti-mouse Alexa Fluor 647). This Lamin C antibody was validated previously in *Drosophila* brains[62]. The tissues were mounted on slides using Fluoroshield mounting medium (Sigma F6182). Confocal images were acquired on Nikon A1 Confocal microscope at 100X magnification. Quantification of percentage of cells with nuclear invaginations and nuclear-cytoplasmic FUS intensities were performed on ImageJ (NIH). Nuclei were considered to be positive for nuclear invagination if the nuclear membrane (Lamin C staining) visibly extended into the nuclear interior as previously described[62].For quantification of number of P525L-RFP puncta per neuron, an ROI was assigned to each cell body and ImageJ threshold tool was

used to convert puncta (>0.3μm) into pixels, followed by measurement of the number of puncta. Data collection and analysis were not performed blind to the conditions of the experiment. No statistical methods were used to pre-determine sample sizes but our sample sizes are similar to those reported in previous publications[10,39].

Survival assay: F1 adult female flies expressing either FUS-WT, R518K and R521C driven by motor neuron driver (D42-gal4) or FUS WT-RFP and FUS P525L-RFP driven by conditional pan-neuronal driver (ElavGS-gal4) were used for survival analyses. For conditional expression, adults were grown on media containing 20mM RU486 (Mifepristone, Cayman Chemicals) to induce transgene expression starting at day-1 post-eclosion. Flies were grown at 25°C and moved to fresh media every 3–4 days. Death was recorded every other day until all flies from the experimental groups were dead. Kaplan-Meier analysis of percentage survival and graphing the survival curve were performed on Prism Graphpad. Data collection and analysis were not performed blind to the conditions of the experiment. No statistical methods were used to pre-determine sample sizes but our sample sizes are similar to those reported in previous publications[39,60,61].

RNA extraction from *Drosophila* heads

Adult heads from transgenic overexpression or RNAi flies under the GMR-gal4 driver were used for RNA extraction. Fly heads were flash-frozen on dry ice and crushed using a pestle followed by lysis in TRIzol. RNA was extracted using bromo-3-chloropropane separation followed by alcohol precipitation. Contamination from genomic DNA was removed by treatment with DNaseI (Invitrogen) in accordance with manufacturer's instructions. 500ng of RNA was used for cDNA synthesis using iScript Select cDNA Synthesis kit (Biorad) followed by quantitative real-time PCR (qRT-PCR) assays performed using iQ Supermix (Bio-rad) following manufacturer's instructions. All reactions were run on StepOnePlus and cycle threshold (Ct) values were used for determining fold change differences by comparative Ct analysis as previously described[63]. Data collection and analysis were not performed blind to the conditions of the experiment. α-tubulin served housekeeping control for normalization of Ct values. *Drosophila* gene-specific primers and probes were designed using PrimerQuest primer design tool (Integrated DNA Technologies) and listed below:

Nup54

Forward: 5'-GAGTGAGCTGACAGAACTCAAG-3'

Reverse: 5'-CTCGGCCAGTTTCCGTTTAT-3'

Probe: 5'-CCACTGCCACAGCGAAGATACTTGA-3'

Nup62

Forward: 5'-CTTGCTGTTGTCTGCATCTC-3'

Reverse: 5'-CAGCACCAGCTTCAGGA-3'

Probe: 5'-ACATTCTCTTTCGGAACACCGGCA-3'

Nup98

Forward: 5'-GTCTTCTTCGGCAAGGAAATG-3'

Reverse:5’-TCGTCGTCGGGATAAATGATAA-3’

Probe: 5’-ACCTCGATG/ZEN/AGATTGTCCACTTTCGC-3’

Nup214

Forward: 5’-CCTAAGTGAGGACAAGGATGAG-3’

Reverse: 5’-GGCATAGTCTGCAGCTTCTT-3’

Probe: 5’-TGCCTTCGACACTTCTACAACGCA-3’

α-tubulin

Forward: 5’-ACCAGCCTGACCAACATG-3’

Reverse: 5’-CCTCGAAATCGTAGCTCTACAC-3’

Probe: 5’-TCACACGCGACAAGGAAAATTCACAGA-3’

Human Tissue Staining

Formalin fixed paraffin embedded tissue sections (5μm thick) were acquired through the Alzheimer’s Disease Research Center at the Massachusetts General Hospital (Charlestown, MA) or the University of British Columbia ([41], Vancouver, Canada). Available demographics information for the three de-identified cases used in the current study can be found in Supplemental Table 1. Tissues were stained and processed by multiple approaches. For the images in the main text Figure 7, the protocol described in Lee et al was used with anti-FUS (Sigma Aldrich, HPA008784), together with either a hematoxylin nuclear counterstain for immunohistochemistry or a DAPI nuclear counterstain for immunofluorescence[64]. For the images in Supplemental Figure 17, mouse anti-Nup62 (BD Bioscience, BDB610497) was diluted to 1:150[47]. Immunohistochemistry was performed using the Dako Omnis automated immunostainer with primary incubation for 60 mins following heat-induced antigen retrieval and developed using Dako Envision Flex/HRP. Data collection and analysis were not performed blind to the conditions of the experiment

Statistical analysis

For iPSC-based experiments, at least three independent differentiations were performed for all the analyses. One-way ANOVA with multiple comparisons test was performed for analyzing more than two cell lines. Unpaired two-tailed t-test was used across for analyzing differences between the isogenic lines. For fly-based experiments, the following tests were used: Two-tailed unpaired t-test, One-way ANOVA with Tukey’s multiple comparison, Kruskal-Wallis test with Dunn’s multiple comparison and Log-Rank Mantel-Cox test. Error bars represent standard error of the mean (s.e.m.) for cell culture and fly data, and standard deviation for *in vitro* biochemical data. Statistical analyses were calculated using GraphPad Prism v8.1.2. The test used and resulting p-values are indicated for each analysis in the corresponding figure legend.

Randomization was not applied to the experiments herein. For *Drosophila* studies, the different experimental groups refer to independent genotypes; therefore, there was no

randomization used in data sampling. Appropriate controls were always included alongside the experimental conditions.

Supplementary Material

Refer to Web version on PubMed Central for supplementary material.

ACKNOWLEDGMENTS

We thank Dr. Claudia Fallini and Dr. Sapun Parekh for helpful discussion on the manuscript. We are thankful to following investigators and facilities for providing iPSC lines: Dr. Robert Baloh and the Induced Pluripotent Stem Cell Core at Cedars Sinai, Dr. Kevin Eggan (Harvard Medical School), Dr. Fen-Biao Gao (University of Massachusetts Medical School), Dr. Nicholas Maragakis and the Ansari ALS Stem Cell Core at Johns Hopkins, Dr. Ludo Van Den Bosch (Vlaams Instituut voor Biotechnologie), Target ALS and Rutgers University-based core facility (RUCDR). We gratefully acknowledge the contribution of the Cellular Engineering Service at The Jackson Laboratory for expert assistance gene-editing of iPSCs described in this manuscript. We thank Dr. Jeanne McKeon for assistance with cell culture, Ms. Anastasia Murthy for advice on recombinant MBP-FUS protein, and Dr. Mathias Hammer for help with microscopy. We are grateful to the following funding sources: US National Institutes of Health / National Institute on Neurological Disorders and Stroke R01 NS078145 (DAB), R01 NS108769 (DAB and DG), R21 NS091860 (DAB), R01 NS081303 (UBP), R21 NS101661, NS111768, AG064940, NS100055, Muscular Dystrophy Association, the ALS Association, and the Robert Packard Center for ALS at Johns Hopkins (UBP), NIGMS R01GM118530 (NLF), Human Frontier Science Program RGP0045/2018 (NLF), NSF 1845734 (NLF), U01 DA047733 (DG), GM123541 (DG) and NSF 1917206 (DG).

Data availability statement:

No data sets that require mandatory deposition into a public database were generated during the current study. Any data generated and/or analyzed during the current study are available from the corresponding author (DAB) on reasonable request.

REFERENCES

1. Frey S, Richter RP & Görlich D FG-Rich Repeats of Nuclear Pore Proteins Form a Three-Dimensional Meshwork with Hydrogel-Like Properties. Science 314, 815–817 (2006). [PubMed: 17082456]
2. Ryan VH & Fawzi NL Physiological, Pathological, and Targetable Membraneless Organelles in Neurons. Trends in Neurosciences 42, 693–708 (2019). [PubMed: 31493925]
3. Schmidt HB & Görlich D Transport Selectivity of Nuclear Pores, Phase Separation, and Membraneless Organelles. Trends Biochem. Sci 41, 46–61 (2016). [PubMed: 26705895]
4. D'Angelo MA, Raices M, Panowski SH & Hetzer MW Age-dependent deterioration of nuclear pore complexes causes a loss of nuclear integrity in postmitotic cells. Cell 136, 284–295 (2009). [PubMed: 19167330]
5. Mertens J et al. Directly Reprogrammed Human Neurons Retain Aging-Associated Transcriptomic Signatures and Reveal Age-Related Nucleocytoplasmic Defects. Stem Cell 17, 705–718 (2015).
6. Daigle N et al. Nuclear pore complexes form immobile networks and have a very low turnover in live mammalian cells. J. Cell Biol 154, 71–84 (2001). [PubMed: 11448991]
7. Toyama BH et al. Identification of Long-Lived Proteins Reveals Exceptional Stability of Essential Cellular Structures. Cell 154, 971–982 (2013). [PubMed: 23993091]
8. Sugiyama K et al. Calpain-Dependent Degradation of Nucleoporins Contributes to Motor Neuron Death in a Mouse Model of Chronic Excitotoxicity. J. Neurosci 37, 8830–8844 (2017). [PubMed: 28821644]
9. Hutten S & Dormann D Nucleocytoplasmic transport defects in neurodegeneration — Cause or consequence? Seminars in Cell & Developmental Biology (2019).
10. Freibaum BD et al. GGGGCC repeat expansion in C9orf72 compromises nucleocytoplasmic transport. Nature 525, 129–133 (2015). [PubMed: 26308899]

11. Zhang K et al. The C9orf72 repeat expansion disrupts nucleocytoplasmic transport. Nature 525, 56–61 (2015). [PubMed: 26308891]
12. Jovičić A et al. Modifiers of C9orf72 dipeptide repeat toxicity connect nucleocytoplasmic transport defects to FTD/ALS. Nat Neurosci 18, 1226–1229 (2015). [PubMed: 26308983]
13. Boeynaems S et al. Drosophila screen connects nuclear transport genes to DPR pathology in c9ALS/FTD. Sci Rep 6, 20877 (2016). [PubMed: 26869068]
14. Coyne AN et al. G4C2 Repeat RNA Initiates a POM121-Mediated Reduction in Specific Nucleoporins in C9orf72 ALS/FTD. Neuron 107, 1124–1440 (2020). [PubMed: 32673563]
15. Chou C-C et al. TDP-43 pathology disrupts nuclear pore complexes and nucleocytoplasmic transport in ALS/FTD. Nat Neurosci 79, 1 (2018).
16. Giampetruzzi A et al. Modulation of actin polymerization affects nucleocytoplasmic transport in multiple forms of amyotrophic lateral sclerosis. Nature Communications 10, 3827–15 (2019).
17. Sama RRK, Ward CL & Bosco DA Functions of FUS/TLS from DNA repair to stress response: implications for ALS. ASN Neuro 6, 1–18 (2014).
18. Dormann D et al. ALS-associated fused in sarcoma (FUS) mutations disrupt Transportin-mediated nuclear import. EMBO J. 29, 2841–2857 (2010). [PubMed: 20606625]
19. Woerner AC et al. Cytoplasmic protein aggregates interfere with nucleocytoplasmic transport of protein and RNA. Science 351, 173–176 (2016). [PubMed: 26634439]
20. Görlich D & Mattaj IW Nucleocytoplasmic transport. Science 271, 1513–1518 (1996). [PubMed: 8599106]
21. Kodiha M, Chu A, Matusiewicz N & Stochaj U Multiple mechanisms promote the inhibition of classical nuclear import upon exposure to severe oxidative stress. Cell Death Differ. 11, 862–874 (2004). [PubMed: 15088071]
22. Bosco DA et al. Mutant FUS proteins that cause amyotrophic lateral sclerosis incorporate into stress granules. Hum. Mol. Genet 19, 4160–4175 (2010). [PubMed: 20699327]
23. Baron DM et al. Quantitative proteomics identifies proteins that resist translational repression and become dysregulated in ALS-FUS. Hum. Mol. Genet 28, 2143–2160 (2019). [PubMed: 30806671]
24. Cassany A & Gerace L Reconstitution of nuclear import in permeabilized cells. Methods Mol. Biol 464, 181–205 (2009). [PubMed: 18951186]
25. Tischbein M et al. The RNA-binding protein FUS/TLS undergoes calcium-mediated nuclear egress during excitotoxic stress and is required for GRIA2 mRNA processing. J. Biol. Chem 294, 10194–10210 (2019). [PubMed: 31092554]
26. Kaushansky LJ Investigating the Effects of Mutant FUS on Stress Response in Amyotrophic Lateral Sclerosis. Master Thesis. University of Massachusetts Medical School. (2015). (https://escholarship.umassmed.edu/gsbs_diss/792/)
27. Khosravi B et al. Cytoplasmic poly-GA aggregates impair nuclear import of TDP-43 in C9orf72ALS/FTLD. Hum. Mol. Genet 26, 790–800 (2016).
28. Wang H et al. Mutant FUS causes DNA ligation defects to inhibit oxidative damage repair in Amyotrophic Lateral Sclerosis. Nature Communications 9, 3683–18 (2018).
29. Kamelgarn M et al. Proteomic analysis of FUS interacting proteins provides insights into FUS function and its role in ALS. Biochim. Biophys. Acta 1862, 2004–2014 (2016). [PubMed: 27460707]
30. Burke KA, Janke AM, Rhine CL & Fawzi NL Residue-by-Residue View of In Vitro FUS Granules that Bind the C-Terminal Domain of RNA Polymerase II. Mol. Cell 60, 231–241 (2015). [PubMed: 26455390]
31. Murakami T et al. ALS/FTD Mutation-Induced Phase Transition of FUS Liquid Droplets and Reversible Hydrogels into Irreversible Hydrogels Impairs RNP Granule Function. Neuron 88, 678–690 (2015). [PubMed: 26526393]
32. Maharana S et al. RNA buffers the phase separation behavior of prion-like RNA binding proteins. Science 360, 918–921 (2018). [PubMed: 29650702]
33. Protter DSW et al. Intrinsically Disordered Regions Can Contribute Promiscuous Interactions to RNP Granule Assembly. Cell Rep 22, 1401–1412 (2018). [PubMed: 29425497]

34. Davis LI & Blobel G Nuclear pore complex contains a family of glycoproteins that includes p62: glycosylation through a previously unidentified cellular pathway. Proc. Natl. Acad. Sci. U.S.A 84, 7552–7556 (1987). [PubMed: 3313397]
35. Cordes VC, Reidenbach S & Franke WW Cytoplasmic annulate lamellae in cultured cells: composition, distribution, and mitotic behavior. Cell Tissue Res. 284, 177–191 (1996). [PubMed: 8625385]
36. Underwood JM, Becker KA, Stein GS & Nickerson JA The Ultrastructural Signature of Human Embryonic Stem Cells. J. Cell. Biochem 118, 764–774 (2017). [PubMed: 27632380]
37. Sama RRK et al. ALS-linked FUS exerts a gain of toxic function involving aberrant p38 MAPK activation. Sci Rep 7, 115–13 (2017). [PubMed: 28273913]
38. Lanson NA et al. A Drosophila model of FUS-related neurodegeneration reveals genetic interaction between FUS and TDP-43. Hum. Mol. Genet 20, 2510–2523 (2011). [PubMed: 21487023]
39. Casci I et al. Muscleblind acts as a modifier of FUS toxicity by modulating stress granule dynamics and SMN localization. Nature Communications 10, 5583–20 (2019).
40. Chen Y et al. Expression of human FUS protein in Drosophila leads to progressive neurodegeneration. Protein Cell 2, 477–486 (2011). [PubMed: 21748598]
41. Rademakers R et al. Fusgene mutations in familial and sporadic amyotrophic lateral sclerosis. Muscle Nerve 42, 170–176 (2010). [PubMed: 20544928]
42. Şahin A et al. Human SOD1 ALS Mutations in a Drosophila Knock-In Model Cause Severe Phenotypes and Reveal Dosage-Sensitive Gain- and Loss-of-Function Components. Genetics 205, 707–723 (2017). [PubMed: 27974499]
43. Shi KY et al. Toxic PRn poly-dipeptides encoded by the C9orf72 repeat expansion block nuclear import and export. Proc. Natl. Acad. Sci. U.S.A 114, 1111–1117 (2017). [PubMed: 28096423]
44. Vanneste J et al. C9orf72-generated poly-GR and poly-PR do not directly interfere with nucleocytoplasmic transport. Sci Rep 9, 15728–10 (2019). [PubMed: 31673013]
45. Mann JR et al. RNA Binding Antagonizes Neurotoxic Phase Transitions of TDP-43. Neuron 102, 321–338.e8 (2019). [PubMed: 30826182]
46. Kamelgarn M et al. ALS mutations of FUS suppress protein translation and disrupt the regulation of nonsense-mediated decay. Proceedings of the National Academy of Sciences 115, E11904–E11913 (2018).
47. Yamashita T, Aizawa H, Teramoto S, Akamatsu M & Kwak S Calpain-dependent disruption of nucleo-cytoplasmic transport in ALS motor neurons. Sci Rep 7, 3643 (2017). [PubMed: 28623286]
48. Ibarra A & Hetzer MW Nuclear pore proteins and the control of genome functions. Genes Dev. 29, 337–349 (2015). [PubMed: 25691464]
49. Archbold HC et al. TDP43 nuclear export and neurodegeneration in models of amyotrophic lateral sclerosis and frontotemporal dementia. Sci Rep 8, 920 (2018). [PubMed: 29343842]
50. Steyaert J et al. FUS-induced neurotoxicity in Drosophila is prevented by downregulating nucleocytoplasmic transport proteins. Hum. Mol. Genet 27, 4103–4116 (2018). [PubMed: 30379317]
51. Ng S-Y et al. Genome-wide RNA-Seq of Human Motor Neurons Implicates Selective ER Stress Activation in Spinal Muscular Atrophy. Cell Stem Cell 17, 569–584 (2015). [PubMed: 26321202]
52. Skarnes WC, Pellegrino E & McDonough JA Improving homology-directed repair efficiency in human stem cells. Methods 164–165, 18–28 (2019).
53. Baron DM et al. Amyotrophic lateral sclerosis-linked FUS/TLS alters stress granule assembly and dynamics. Molecular Neurodegeneration 2016 11:1 8, 30–18 (2013).
54. Stoica R et al. ALS/FTD associated FUS activates GSK 3β to disrupt the VAPB-PTPIP51 interaction and ER-mitochondria associations. EMBO Reports 17, 1326–1342 (2016). [PubMed: 27418313]
55. An H et al. ALS-linked FUS mutations confer loss and gain of function in the nucleus by promoting excessive formation of dysfunctional paraspeckles. Acta Neuropathol Commun 7, 1–14 (2019). [PubMed: 30606247]

56. Koulouras G et al. EasyFRAP-web: a web-based tool for the analysis of fluorescence recovery after photobleaching data. Nucleic Acids Res. 46, W467–W472 (2018). [PubMed: 29901776]
57. Eftekharzadeh B et al. Tau Protein Disrupts Nucleocytoplasmic Transport in Alzheimer's Disease. Neuron 99, 925–940.e7 (2018). [PubMed: 30189209]
58. Monahan Z et al. Phosphorylation of the FUS low-complexity domain disrupts phase separation, aggregation, and toxicity. EMBO J. 36, 2951–2967 (2017). [PubMed: 28790177]
59. Pandey UB et al. HDAC6 rescues neurodegeneration and provides an essential link between autophagy and the UPS. Nature 447, 859–863 (2007). [PubMed: 17568747]
60. Ramesh N et al. RNA dependent suppression of C9orf72 ALS/FTD associated neurodegeneration by Matrin-3. Acta Neuropathol Commun 8, 1182 (2020).
61. Ortega JA et al. Nucleocytoplasmic Proteomic Analysis Uncovers eRF1 and Nonsense-Mediated Decay as Modifiers of ALS/FTD C9orf72 Toxicity. Neuron 106, 90–107.e13 (2020). [PubMed: 32059759]
62. Frost B, Bardai FH & Feany MB Lamin Dysfunction Mediates Neurodegeneration in Tauopathies. Current biology : CB 26, 129–136 (2016). [PubMed: 26725200]
63. Schmittgen TD & Livak KJ Analyzing real-time PCR data by the comparative C(T) method. Nat Protoc 3, 1101–1108 (2008). [PubMed: 18546601]
64. Lee EB et al. Expansion of the classification of FTLD-TDP: distinct pathology associated with rapidly progressive frontotemporal degeneration. Acta Neuropathol 134, 65–78 (2017). [PubMed: 28130640]

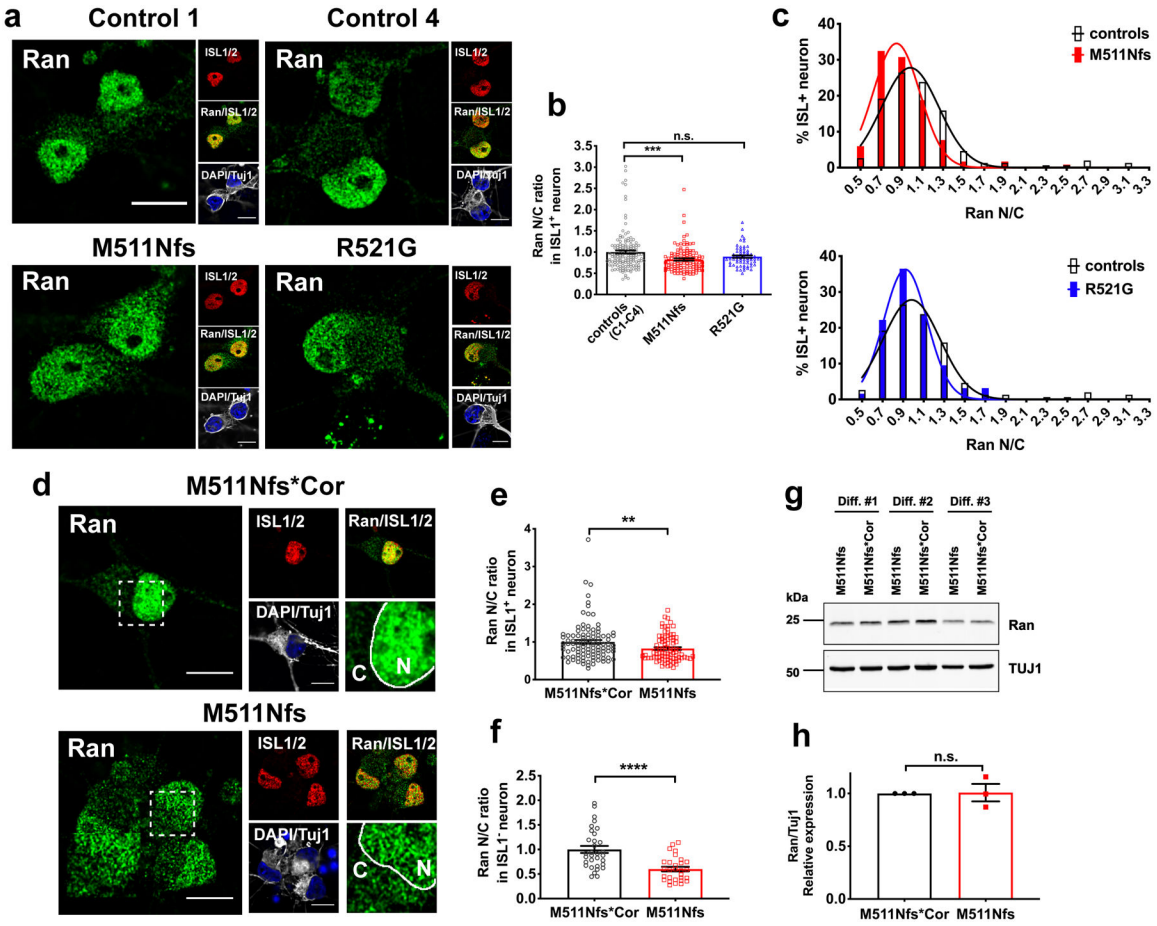

Figure 1. The Ran gradient is perturbed in motor neurons expressing ALS-linked FUS.

Immunofluorescence imaging of Ran revealed enhanced cytoplasmic versus nuclear Ran localization in FUS M511Nfs iPSC-derived motor neurons compared to control and FUS R521G motor neurons. Neurons at DIV 36–42 were used and the indicated number of cells (below) were analyzed across at least three independent differentiations (each differentiation represents an experiment). (**a-c**) Four control (C1–C4) and two ALS (M511Nfs and R521G) lines were employed (**a**) Representative immunofluorescence images for neurons derived from two control and two ALS iPSC lines. Staining includes Ran (green), the motor neuron marker Islet1/2 (red), the pan-neuronal marker Tuj1 (anti-TUBB3; grey), and DAPI (blue). Scale bar= 10 μm. The Ran N/C ratio of the chosen representative neurons: C1 (1.25 and 1.53); C4 (2.12, 0.99); M511Nfs (0.64, 0.69); R521G (1.29). (**b,c**) Quantification of Ran N/C ratio in all six lines (pooled controls, n=151; M511Nfs, n=117; R521G, n=63 cells) reveals a significant decrease for FUS M511Nfs neurons. Each point in the bar graph represents the average across all cells for an independent experiment. Within each experiment, the ALS lines were normalized to the control lines. One-way ANOVA with Dunnett's multiple comparisons test, ***p=0.0003, n.s. p=0.0967. F (2, 328)= 7.632. Error bars represent s.e.m. (**c**) Frequency distribution graphs of Ran N/C ratio for FUS M511Nfs (left) and R521G (right) neurons compared to controls. (**d-f**) Similar analysis as A-D using FUS M511Nfs motor neurons compared to the isogenic, corrected control (M511Nfs*Cor). (**d**) Immunofluorescence staining as in (a). Scale bar= 10 μm.

The Ran N/C ratio of the chosen representative neurons: M511Nfs*Cor (1.19); M511Nfs (0.55, 0.58, 0.91). Abbreviation within the zoom insets: N (nucleus), C (cytoplasm). (**e**) Quantification of the Ran N/C ratio as in (b). Ran N/C is significantly lower in M511Nfs versus M511Nfs*Cor neurons (M511Nfs*Cor, n=103; M511Nfs, n=90 cells). Unpaired two-tailed t-test, **p=0.0063. t=2.762, df=191. (**f**) Quantification of the Ran N/C ratio in ISL1/2 negative M511Nfs and M511Nfs*Cor neurons (non-motor neurons). Ran N/C is significantly lower in M511Nfs versus M511Nfs*Cor neurons (M511Nfs*Cor, n=32; M511Nfs, n=29 cells). Unpaired two-tailed t-test, ****p<0.0001. t=4.594, df=59. (**g**) A Western blot analysis of total Ran protein levels in neurons derived from the indicated line; data from three independent differentiations are shown. Tuj1 was used as loading control. Source data are provided as a Source Data file. (**h**) Quantification of (g). Unpaired two-tailed t-test, n.s.= not significant. t=0.09654, df=4. For all quantifications, data distribution was assumed to be normal but this was not formally tested.

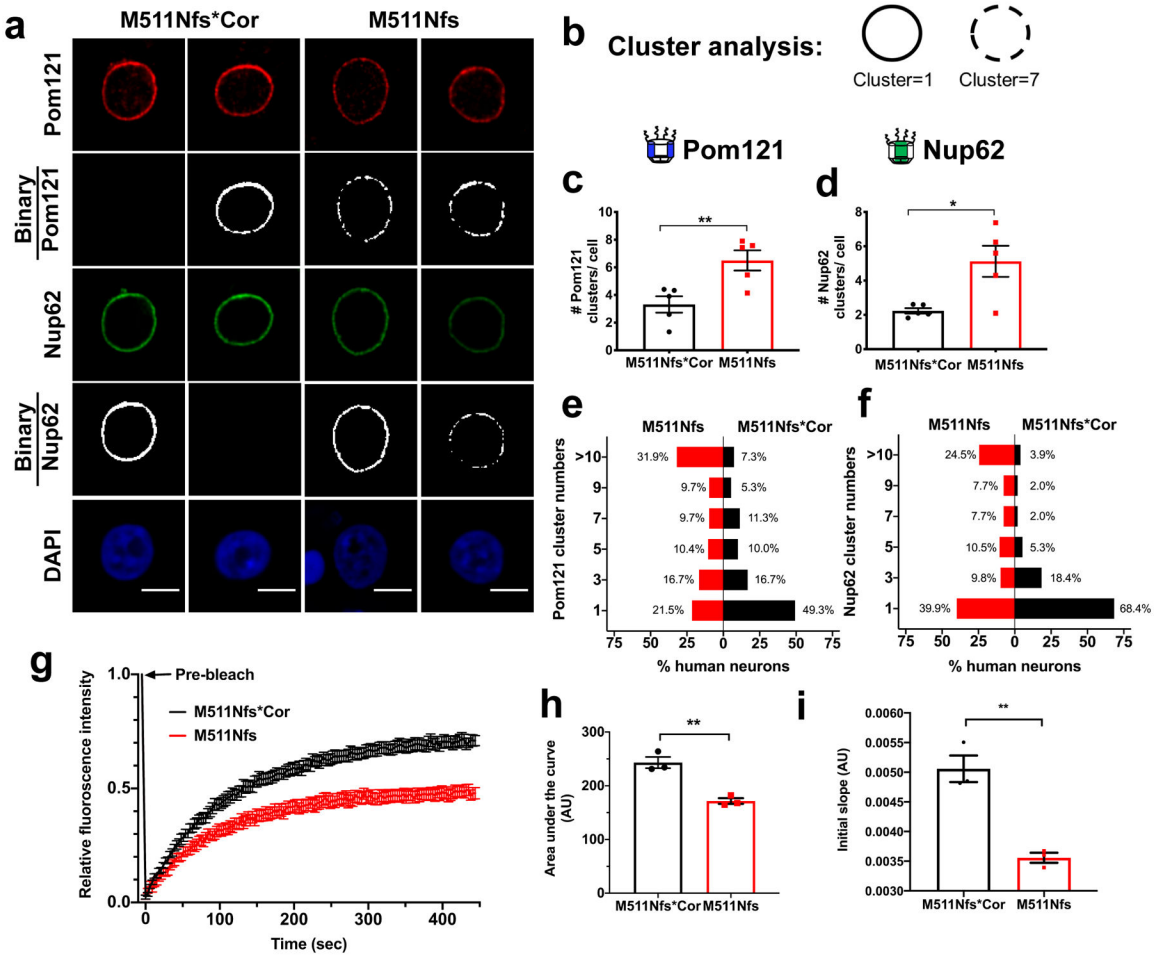

Figure 2. Diminished nuclear pore signal and nucleocytoplasmic transport in ALS-FUS human neurons.

(**a**) Immunofluorescence images of Pom121 (red) and Nup62 (green), representative of n=5 experiments, reveals weaker signals in FUS M511Nfs nuclei compared to nuclei from the isogenic control neurons. Binary images (white) derived from the fluorescence images are shown. DAPI (blue). Scale bar = 5 μm. (**b**) An illustration for the cluster analysis used to quantify the continuity of Pom121 and Nup62 staining around the perimeter of the nucleus. (**c-f**) Results of the cluster analysis for Pom121 (scaffold Nup; **c, e**) and Nup62 (central channel Nup; **d, f**) for n=152 M511Nfs*Cor and n=144 M511Nfs nuclei that were analyzed across five independent differentiations (each differentiation represents an experiment) from neurons at DIV 36–45. (**c, d**): significantly higher cluster numbers in FUS M511Nfs versus M511Nfs*Cor nuclei through analysis of Pom121 (Unpaired two-tailed t-test, **p=0.0095, t=3.391, df=8) and Nup62 (Unpaired two-tailed t-test, p=0.0137, t=3.144, df=8; error bars represent s.e.m.). (**e, f**): results of the cluster analysis presented in a population pyramid format show the cluster number for every neuron analyzed. Each point in a bar graph represents the average across all cells in that experiment, normalized to M511Nfs*Cor. (**g-i**) Results of the FRAP experiment with the NLS-tdTomato-NES shuttling reporter in FUS M511Nfs*Cor neurons (black; n=29 cells) and M511Nfs neurons (red; n=36 cells) across three independent differentiations. Neurons at DIV 56–60 were used for

FRAP experiments. (**g**) FRAP recovery curves. (**h**) The area under the recovery curve was significantly lower in FUS M511Nfs neurons compared to M511Nfs*Cor neurons (Unpaired two-tailed t-test, **p=0.0036, t=6.112, df=4; error bars represent s.e.m.). Each point in the bar graph represents an independent differentiation. (**i**) The initial slopes of the FRAP recovery curves (comprising the first 50 seconds from panel **g**) were determined using a non-linear regression analysis and found to be significantly slower in FUS M511Nfs neurons compared to M511Nfs*Cor neurons (Unpaired two-tailed t-test, **p=0.0033, t=6.271, df=4; error bars represent s.e.m.). For all quantifications, data distribution was assumed to be normal but this was not formally tested.

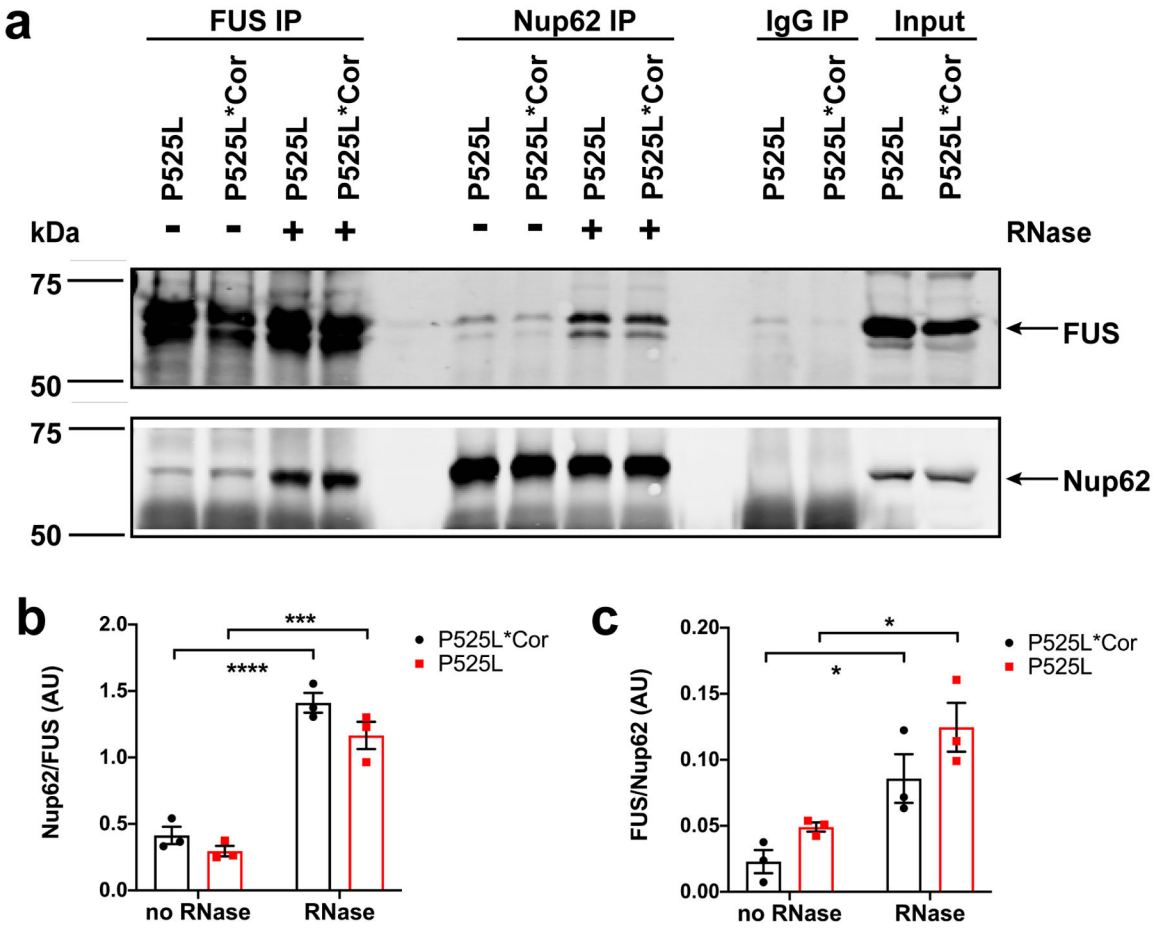

Figure 3. Wild-type and mutant FUS interact with Nup62 in iPSCs.

(**a**) Left: FUS IP. Nup62 was pulled down with wild-type (P525L*Cor) and mutant (P525L) FUS. Middle: Nup62 IP. Both wild-type and mutant FUS were pulled down with Nup62. In both IPs, interactions of FUS and Nup62 were retained and significantly enhanced upon RNase treatment, suggesting the interactions were not mediated through RNA. Right: IgG and input controls for IP. Source data are provided as a Source Data file. (**b**) Quantification for FUS IP. Densitometry analysis of FUS and Nup62 signals in the Western blot shown in (a). Two-way ANOVA with Tukey's multiple comparisons test. P525L*Cor: ****p<0.0001; P525L: ***p=0.0002. F (1, 8)=0.7543. (**c**) Quantification for Nup62 IP, as described for (b). Two-way ANOVA with Tukey's multiple comparisons test. P525L*Cor: *p=0.0497; P525L: *p=0.0204. F (1, 8)=0.2072. Only significant comparisons were denoted. (**b,c**) Each point in the bar graph represents a biological replicate (n=3). Error bars represent s.e.m. Data distribution was assumed to be normal but this was not formally tested.

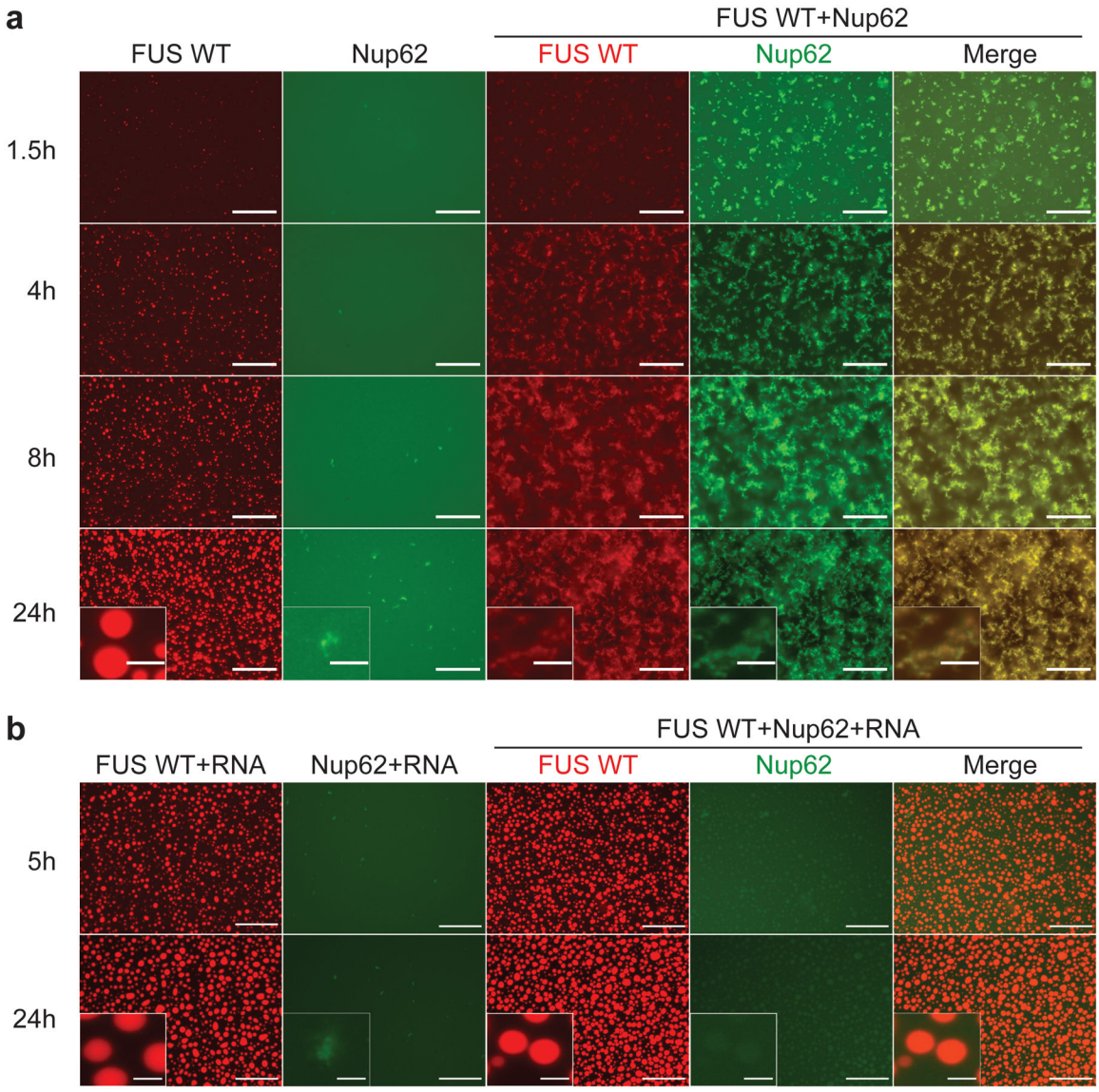

Figure 4. Nup62 and FUS alter the phase separation properties of each other in a manner that is modulated by RNA *in vitro*.

Fluorescence images showing phase separation of 1.5 μM MBP-FUS WT (red) doped with ≤2.5% Alexa555-labelled MBP-FUS WT and 1.5 μM MBP-Nup62 (green) doped with ≤ 2.7% Alexa488-labelled MBP-Nup62. Full-length FUS and Nup62 proteins were used herein. (**a**) MBP-FUS forms dynamic spherical droplets (Supplemental Video 1). Co-mixing MBP-FUS with MBP-Nup62 promotes the formation of FUS/Nup62-containing amorphous assemblies that appear less dynamic (Supplemental Video 2). (**b**) Co-mixing as in (a) in the presence of RNA (mass ratio of RNA:FUS:Nup62 ≈ 1.5:1:1) prevents the formation of amorphous assemblies, giving way to spherical droplets MBP-FUS with some MBP-Nup62 co-localization. Images were taken at the indicated timepoints after initiation of phase separation by 3.6% PEG. Results are representative of n=4 independent experiments. Scale bar= 50 μm (inset = 5 μm).

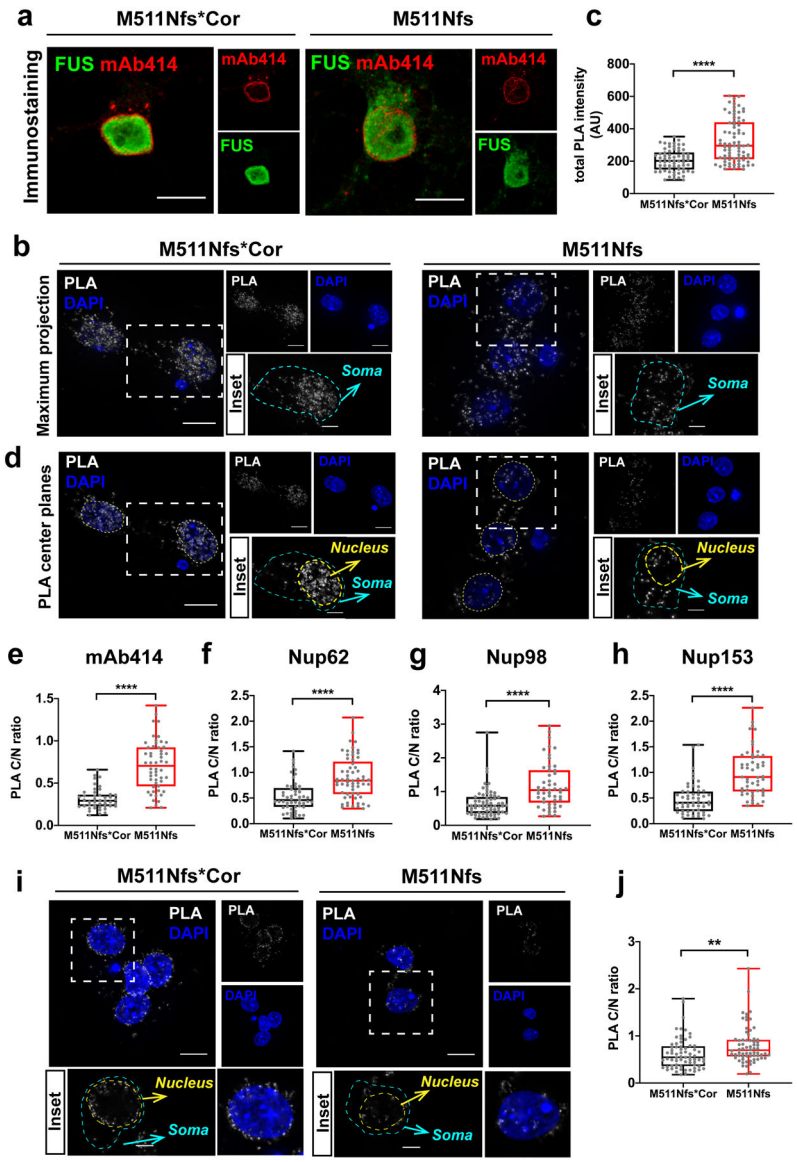

Figure 5. Mutant FUS interacts with F/G Nup in the cytoplasm of human neurons.

(**a**) Immunofluorescence images of FUS (green) and F/G Nup marker mAb414 (red) in human neurons are representative of n=3 experiments. Tuj1 (grey). DAPI (blue). Scale bar= 10 μm. (**b**) Proximity ligation assay (PLA) using the FUS and mAb414 antibodies in (a). (**b**) Maximum intensity projections of the all z-planes for cell soma (delineated with blue dotted line). (**c**) Quantification of (b). A significant increase of total PLA signal in FUS M511Nfs neurons compared to control neurons; ****p<0.0001. t=6.630, df=141. (**d**) Maximum intensity projections of the center ten optical planes, allowing for quantification of nuclear (delineated with yellow dotted line surrounding DAPI) versus cytoplasmic PLA signals detected in between the blue and yellow lines. PLA signal at the nuclear membrane is counted as “nuclear” here. (**e**) Quantification of (d). PLA C/N ratio revealed significantly higher cytoplasmic PLA signal in FUS M511Nfs neurons compared to control neurons; ****p<0.0001. t=8.384, df=97. The PLA C/N ratio of the chosen representative neurons:

M511Nfs*Cor (0.33, 0.30); M511Nfs (1.05, 1.00, 1.42). (**f-h**) Similar PLA C/N analyses were performed with FUS and Nup62 (f), Nup98 (g), Nup153 (h) antibodies. ****p<0.0001. (f) t=5.240, df=112. (g) t=5.142, df=114. (h) t=6.797, df=102. (**i**) PLA analysis with mAb414 and Nup62 antibodies show a loss of nuclear Nup PLA signal (including the nuclear membrane) and an increase of cytoplasmic Nup PLA signal in FUS M511Nfs neurons compared to the control. PLA signal (grey); DAPI (Blue). The PLA C/N ratio of the chosen representative neurons: M511Nfs*Cor (0.49, 0.27, 0.18); M511Nfs (0.71, 1.49). (**j**) Quantification of (i). M511Nfs*Cor, n=69; M511Nfs, n=68 cells; **p=0.0018. t=2.832, df=135. All the images were chosen to be representative of the mean quantified value. Scale bar= 10 μm. (**c,e,f,h,j**) Box and whiskers plot showing all cells analyzed from three independent differentiations. Plots indicate the 25^{th} (above) and 75^{th} (below) percentiles, with a line within showing the median; whiskers above and below the box indicate the maximum and minimum values. Unpaired two-tailed t-test was used for all comparisons. Data distribution was assumed to be normal but this was not formally tested.

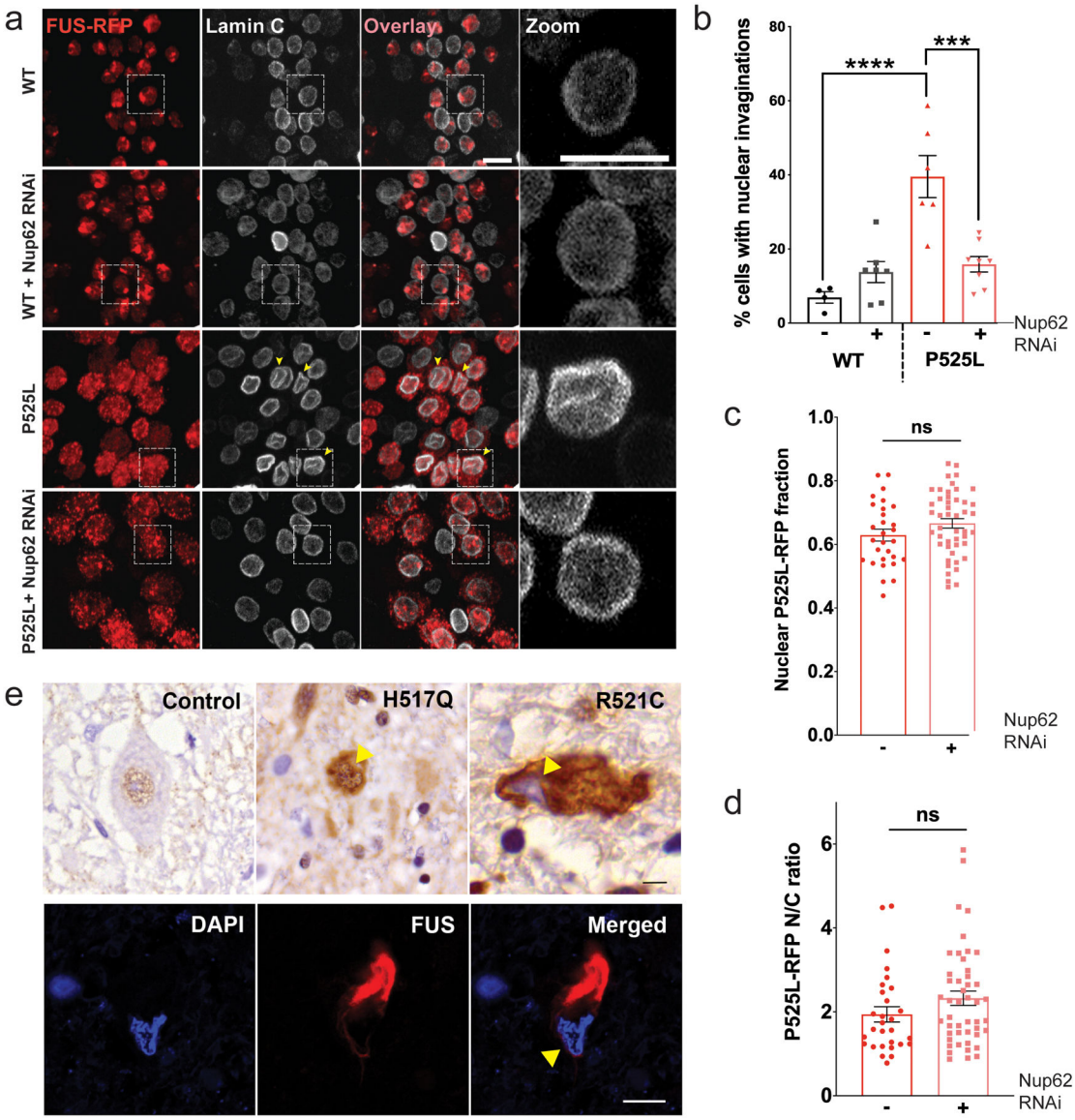

Figure 6. Nuclear abnormalities associated with ALS-linked FUS are rescued by knock-down of Nup62 *in vivo*

(a) Immunofluorescence imaging of larval ventral nerve chord in *Drosophila* expressing FUS WT-RFP (red, top) and ALS mutant FUS P525L-RFP (red, bottom), with and without Nup62 knockdown. Lamin C (grey) staining was used to mark the nuclear membrane. Nuclear membrane invaginations, which appear as wrinkled membranes, were observed in P525L-expressing neurons (denoted by yellow arrowheads). Zoom images show normal nuclear membrane morphologies for all conditions except P525L. Scale bar= 10μm. **(b)** Quantification of percentage of neurons that have nuclear membrane defects in all four groups (Each point in the bar graph represents an animal. FUS WT, n=4; FUS WT + Nup62 RNAi, n=7; FUS P525L, n=6; FUS P525L + Nup62 RNAi n=8) reveals a significant increase in percentage of neurons with nuclear morphology defects in P525L-expressing neurons compared to WT. Upon Nup62 knockdown, there was a significant decrease in percentage of P525L-expressing neurons with nuclear morphology defects. Each point

represents data from one larva. One-way ANOVA with Tukey's multiple comparisons test was used for analysis (F-value=14.94, df=3). Only significant comparisons were denoted. WT-RFP vs P525L-RFP ****p-value<0.0001; P525L-RFP vs P525L-RFP + Nup62 RNAi ***p-value=0.0003. Error bars indicate s.e.m. **(c)** Quantification of nuclear FUS-P525L intensities and **(d)** nuclear-cytoplasmic (N/C) ratio of FUS-P525L intensities with and without Nup62 knockdown (P525L-RFP, n=29; P525L + Nup62 RNAi, n=47) indicates no difference in either nuclear levels (p-value=0.128) **(c)**, or nuclear-cytoplasmic FUS distribution (p-value=0.145) **(d)** in P525L-expressing neurons upon Nup62 knockdown. Each point in (c) and (d) represent individual neurons. Unpaired two-tailed Student's t-test was used for analysis (For [c]: t=1.539, df = 74; and for [d]: t=1.473, df = 74). Error bars indicate s.e.m. (**b-d**) Data distribution was assumed to be normal but this was not formally tested. (**e**) Post-mortem human spinal cord from two ALS-FUS cases (H517Q and R521C) compared to a neurologically normal control demonstrate abnormally misshapen nuclei (i.e., deviating from a round shape and/or containing membrane invaginations), which are denoted by yellow arrow-heads. Images are representative of FUS inclusion-bearing neurons within n=1 staining experiments. Tissues were stained with anti-FUS antibody and a nuclear dye, revealing cytoplasmic mislocalization of ALS-FUS. Top panel: immunohistochemistry. Bottom panel: confocal immunofluorescence images of a neuron from the FUS R521C case with FUS accumulation (red) proximal to the nucleus (blue). Scale bar= 10μm.

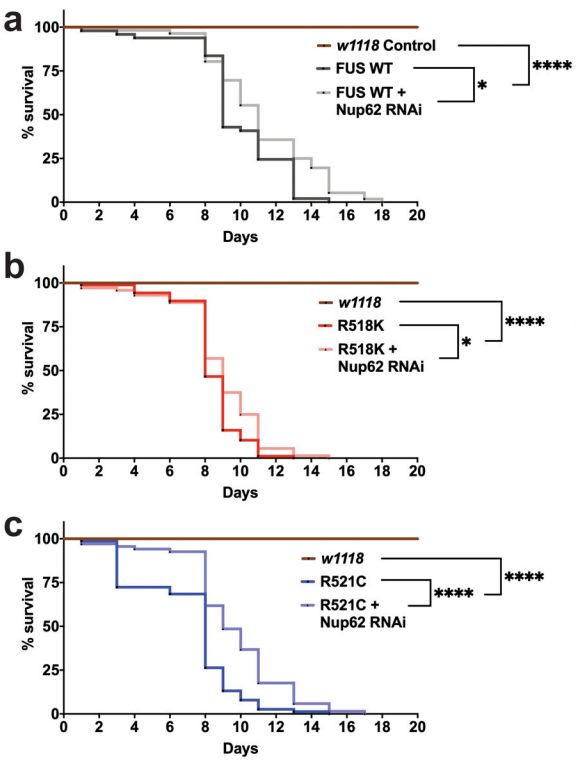

d

	FUS-WT		R518K		R521C	
Nup62 RNAi	-	+	-	+	-	+
25% death	9 days	9 days	8 days	8 days	3 days	8 days(+5)
50% death	9 days	11 days(+2)	8 days	9 days(+1)	8 days	9 days(+1)
75% death	11 days	13 days(+2)	9 days	11 days(+2)	8 days	11 days(+3)

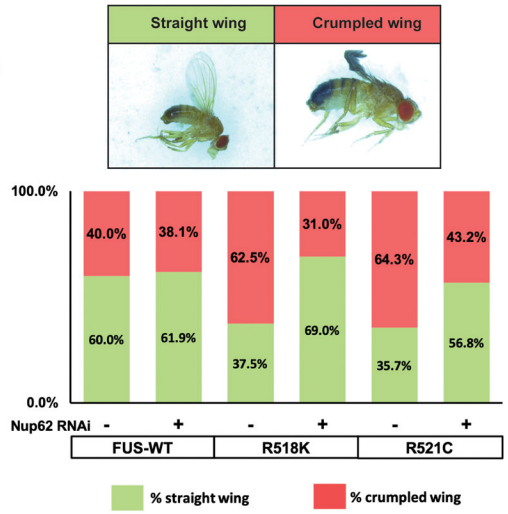

Figure 7. Modulation of Nup expression rescues FUS-induced toxicity *in vivo*.

(a-c) Kaplan-Meier survival curves of flies expressing **(a)** FUS WT, **(b)** R518K mutant and **(c)** R521C mutants with and without Nup62 RNAi in adult motor neurons (D42-gal4). Non-transgenic (*w1118*) flies were used as controls. Log-Rank (Mantel-Cox) statistical test was used for analysis of survival curves. ****p-value<0.0001; FUS-WT vs FUS-WT + Nup62 RNAi p-value=0.0397; R518K vs R518K + Nup62 RNAi p-value=0.0128. Data distribution was assumed to be normal but this was not formally tested. **(d)** Tabular representation of number of days it took for 25%, 50% and 75% death respectively for each genotype. The number of days that Nup62 siRNA confers for survival for each genotype are shown in red. **(e)** Percentage of flies expressing FUS WT, R518K and R521C in motor neurons through development, with and without Nup62 RNAi, knockdown that eclosed/hatched with normal straight wings (green) or abnormal crumpled wings (red) (*w1118* Control n = 99; FUS WT n = 49; FUS WT + Nup62 RNAi n = 56; R518K n=88; R518K + Nup62 RNAi n = 72; R521C n = 76; R521C + Nup62 RNAi n = 68).